CHALMERS
UNIVERSITY OF TECHNOLOGY

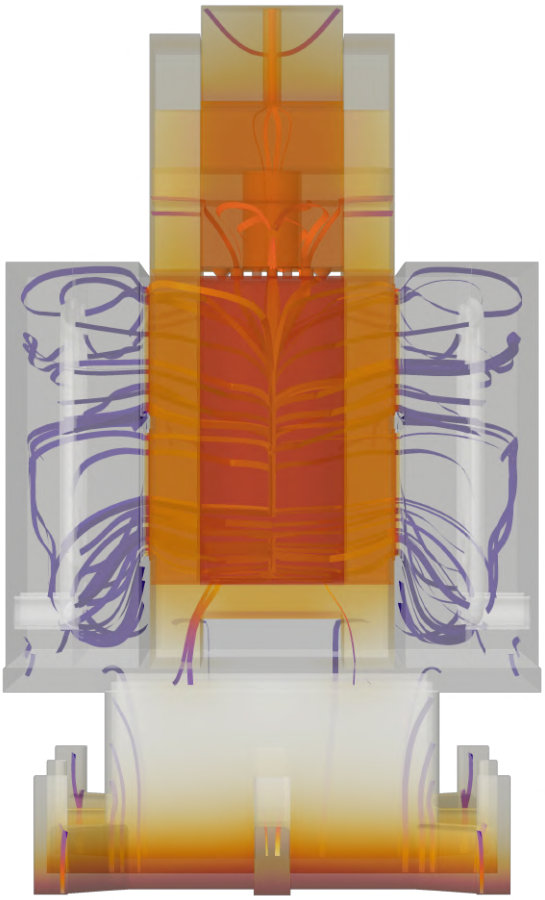

Thermal Modelling of Battery Characterization Techniques

Master's thesis in Sustainable electric power engineering and electromobility &
Master's thesis in Innovative and sustainable chemical engineering

Simen Lindstad & Anton Enochsson

DEPARTMENT OF ELECTRICAL ENGINEERING
CHALMERS UNIVERSITY OF TECHNOLOGY
Gothenburg, Sweden 2026
www.chalmers.se

Master's thesis 2026

Thermal Modelling of Battery Characterization Techniques

Simen Lindstad & Anton Enochsson

CHALMERS
UNIVERSITY OF TECHNOLOGY

Department of Electrical Engineering
Chalmers University of Technology
Gothenburg, Sweden 2026

Experimental Calibration and Numerical Validation of a Vacuum-Based Calorimeter for Measuring Heat Generation in Large-Format Cylindrical Cells
Simen Lindstad & Anton Enochsson

Supervisor: Daniel Poposki, Volvo Group Trucks Technology, Cell Technology
Supervisor: Jan Engelhardt, Denmark Technical University, Institute of Wind and Energy Systems
Supervisor: Chresten Træholt, Denmark Technical University, Institute of Wind and Energy Systems
Supervisor: Chunyang Zhao, Denmark Technical University, Institute of Wind and Energy Systems
Examiner: Torbjörn Thiringer, Chalmers Technical University, Department of Electrical Engineering

Master's Thesis 2026
Department of Electrical Engineering
Division of Electric Power Engineering
Chalmers University of Technology
SE-412 96 Gothenburg
Telephone +46 31 772 1000

Cover: 3D model of heat flow in cylindrical cell in a vacuum-based calorimeter

Typeset in LaTeX
Printed by Chalmers Reproservice
Gothenburg, Sweden 2026

Preface

This master's thesis is the final project of the master's study of Simen Lindstad and Anton Enochsson. Simen Lindstad is graduating in Sustainable Energy Technologies from DTU, with a Nordic-5-Tech exchange year at Chalmers. Anton Enochsson is graduating in Innovative and Sustainable Chemical Engineering from Chalmers. The work has been fairly divided with a 50/50 split. The project was created by Volvo Group Trucks Technology and was formed in collaboration with the supervisor Daniel Poposki (Volvo GTT) and examiner Thorbjörn Thiringer (Chalmers).

The main focus of the thesis is to quantify the change in accuracy and reliability when introducing a calorimeter in a vacuum environment. The motivation for this project was to accurately measure the heat flow from a large-format cylindrical cell from Volvo GTT.

We are proud to present this work as our own, yet the use of artificial intelligence (AI) has been useful for maintaining a high efficiency throughout the work process. Grammarly has been used for correcting punctuation and basic grammar. Google's Gemini has been used for the creation and correction of MATLAB scripts. For every script, the data has been verified to ensure correct handling and intended purpose. AI has mainly been used for its efficiency in producing and fault-checking basic scripts. No AI has been used in the creation of the text.

Simen Lindstad & Anton Enochsson, Gothenburg, 2026

Experimental Calibration and Numerical Validation of a Vacuum-Based Calorimeter for Measuring Heat Generation in Large-Format Cylindrical Cells

SIMEN LINDSTAD & ANTON ENOCHSSON
Department of Electrical Engineering
Chalmers University of Technology

Abstract

The goal of this master's thesis was to calibrate a calorimeter in a vacuum environment and quantify its potential benefits compared to air. The motivation for the project was to record the heat from a cylindrical cell with high accuracy. Peltier elements were used to record the heat flow of the samples' cubical enclosure, each side with a heat sink to maintain a stable cold-side reference.

The initial testing proved unstable and problematic to replicate, motivating four iterations of the setup. Vacuum conditions proved stable, yet time-consuming, requiring 6 hours to reach a steady state, compared to under 2 hours in air. The sensitivity of the Peltier elements was found to be 50-100 mW, yet the full system could only achieve a stable calibration coefficient from 1 W, found to be 19.93 and 19.85 W/V for air and vacuum, respectively.

The main challenges with the calorimeter in vacuum were the high correlation to the surrounding lab temperature and the resulting radiation onto the setup. The added isolation proved to be inefficient. The heat sink's surface was heated up by radiation, corrupting the heat flow signal. The recorded voltage was corrected using a reference cell and baseline voltage.

The digital-twin model reached a 7% deviation, which helped locate the parasitic convection through the power cables, accounting for around 21% of the applied power. It also quantified 170-190 mW of radiative heating onto the heat sinks and 30-80 mW of conductive heat from the plastic stand. Ultimately, the vacuum environment proved challenging with no significant benefit over air. Although convective heat transfer was successfully removed, further changes could potentially improve the sensitivity and stability.

Keywords: Calorimetry, Battery, Cylindrical Cell, Isothermal, Peltier Elements, Vacuum, Digital-Twin, Calibration Coefficient, Steady-State, Radiation

"Did we turn on the vacuum?" — Authors

Acknowledgements

We would like to thank all of the brilliant people who have guided and supported us throughout the work of this master's thesis.

Firstly, we are incredibly grateful to our supervisor, Daniel Poposki, for his unwavering support and constant feedback. We also want to thank our examiner Torbjörn Thiringer for his deep knowledge and for helping us stake out the course of this project. We would also like to thank our supervisors in Denmark, Jan Engelhardt, Chresten Træholt and Chunyang Zhao, for their insightful feedback and interest in this thesis. A very special thanks to Douglas Jutsell Nilson for his incredible, neverending support in the laboratory.

We owe a huge debt of gratitude to the Volvo Group Trucks Technology for the opportunity to pursue such an interesting and special project. Also, a special thanks to the Cell Technology Team for the inclusion in the team and the incredible knowledge that helped us.

Finally, we are incredibly grateful to our friends and family for their strong support through the ups and downs of this project.

Simen Lindstad & Anton Enochsson, Gothenburg, 2026

List of Abbreviations

Below is the list of abbreviations that have been used throughout this thesis listed in alphabetical order:

BTMS	Battery Thermal Management System
EV	Electric Vehicle
HFS	Heat Flux Sensor
IHC	Isothermal Heat Conduction
MHFR	Measured Heat Flow Ration
SOC	State of Charge
SOH	State of Health
TEM	Thermoelectric Module

Contents

1

Introduction

The energy storage sector has, in the last decayed, become a hot topic as a green solution. One sector following this trend is the automotive industry, whose greenhouse gas emissions for the product life cycle make up a large percentage of global emissions [1]. The automotive industry is fully investing in electric vehicles (EVs) as a way to produce cleaner transportation alternatives [2].

A constraint for electric vehicles is the energy storage, charging time, and operational lifetime. Although the specific energy storage of a lithium-ion battery cell has doubled over the past few years, it still can not match that of petrol vehicles [2]. A common denominator for the battery constraints is thermal management, as the performance and lifetime of lithium-ion batteries are highly dependent on the operational temperature.

1.1 Background

Heat generation occurs as energy losses in lithium-ion batteries when being charged or discharged, which increases the temperature of the battery. The underlying cause for these losses are internal resistance, charge transport, and electrochemical reactions [3]. The operating temperature significantly affects the internal electrochemical processes and can lead to accelerated cell degradation. As a result, the overall performance and lifespan of the battery are impacted [4]. In the worst of circumstances, accumulated heat can trigger a thermal runaway, which is a self-accelerating mechanism. If this were to occur, it could cause catastrophic safety hazards in the form of fires and explosions [5]. To ensure safe and long-lasting operation, EVs must use an effective battery thermal management system (BTMS). The BTMS maintains the battery within its optimal temperature range and minimise internal temperature gradients [5].

However, the efficiency and reliability of a BTMS are heavily dependent on its design accuracy. To optimally design a thermal management system, a fundamental understanding of the battery's thermal behaviour is required [3]. This makes accurate thermal parameter characterisation of e.g. the battery's heat generation rate, specific heat capacity, and thermal conductivity strictly necessary [4]. Inaccurate estimations of these thermal parameters can result in either an insufficient cooling

system that compromises vehicle safety, or an oversized system that adds unnecessary weight and cost [3]. Therefore, reliable methods for extracting these thermal characteristics are crucial for the development of next-generation batteries [5].

1.2 Previous work

In this section, previous work on the thermal characterisation of lithium-ion cells is presented. It describes the information known for thermal parameter estimations, but also points out what is missing for the current methodologies.

Hu et al. [6] and Panchal et al. [7] each developed custom-built calorimeters for pouch and prismatic cells respectively. The setups utilised thermoelectric modules (TEMs) and heat flux sensors (HFS) for measuring the generated heat. From respective experiments, they both demonstrate how the usage of TEMs gives cost-effective and highly accurate measurements. However, these setups highly rely on flat cell formats for extrapolating results for the whole surface. This focus causes complications for cylindrical cells whose curvature will cause poor sensor contact.

Worwood et al. [8] point out how the geometry of cylindrical cells presents unique measurement challenges. In reference to pouch cells, the internal temperature gradients are more often complex as the shape causes longer heat transfer pathways inside the cell. Attempts to apply heat flux sensors have been made, both by Drake et al. [9] and Murashko et al. [10], which were proven to be successful in measuring dynamic heat generation rate and entropy change profiles. Though both these methodologies used smaller and localised sensors, which showed to give rise to critical issues concerning environmental heat dissipation.

In an attempt to mitigate heat losses to the surrounding environment, different methodologies have been tried to isolate this problem. Yuan et al. [4] and Sheng et al. [11] showcase conducted calorimetric measurements with the usage of physically insulating materials, such as aerogel and expanded polystyrene, respectively. With these, it was still noted that the occurrence of unmeasured convective heat transfer. These were described as the result of imperfect insulation and the ambient temperature inside the laboratory fluctuating. The persistent heat leakage causes disturbances to the calibration of calorimeter systems as the baseline shifts and measurement noise gets introduced.

Recently, a similar attempt to that presented in this thesis was done by Kozma et al. [12]. They tried to minimise the heat losses from large-format cylindrical cells by using flexible heat sensors in different sizes around the the cell in an attempt to capture the heat in all direction. From this work it was concluded that the larger sensors were better at capturing the heat, where 71% of the heat was shown to flow through the lateral surface. Though one factor that was highlighted in the research was the thermal losses via the connectors, which made up for 19% of the applied heat power.

To conclude the presented works, there is a gap for isothermal heat conduction

(IHC) calorimeters regarding specific optimisation for large-format cylindrical cells. More specifically, there is a need for a metrology that can prevent convective heat transfer.

1.3 Purpose

The primary purpose of this thesis is to design, improve, and modify an custom-build IHC calorimeter. The implemented adaptions are intended to improve the precise heat generation measurement of cylindrical lithium-ion cells. By relocating the experimental setup into a vacuum environment, the objective is to eliminate convective heat transfer, thereby minimising unmeasured thermal losses to the surroundings. This is done to improve methodologies for characterising thermal parameter for lithium-ion cells.

1.4 Scope

The following points describe the scope of the thesis regarding what it specifically includes and its delimitations.

- Development of a thermal physics-based simulation of the large-format cylindrical cell calorimeter setup, modelling the heat transfer behaviour in both air and vacuum environments.
- Physical assembly and modifications of the calorimeter setup, specifically adapted for large-format cylindrical geometries.
- Experimental investigation of calibration coefficients using a dummy cell inside a vacuum chamber to study how vacuum conditions improve thermal losses compared to air.
- Cross-validation of the heat transfer characteristics and calibration coefficients (ϵ) by directly comparing the measured experimental data with the results from the simulated models.
- The experimental scope is strictly limited to the specific custom calorimeter setup available at Chalmers University of Technology. Furthermore, the study focuses exclusively on one single physical dimension of large-format cylindrical cells.
- To maintain an achievable workload and focus on standard operating conditions, all experimental measurements are performed within a cooling temperature window of 15°C to 35°C and an applied heating power of 5 W or lower.
- The physical experiments are limited to testing on a cylindrical dummy cell rather than active lithium-ion batteries. Consequently, electrochemical vari-

ables such as state of charge (SOC) and the effects of battery ageing (state of health, SOH) are ruled out from this research.

1.5 Environmental & ethical aspects

As lithium-ion batteries become increasingly established as a solution for the global transition to a sustainable society, this has led to their rapid commercial growth. However, this has raised valid concerns regarding their environmental footprint and ethical supply chains [13, 14]. For batteries to truly fulfil their potential as a long-term, green energy source, the environmental and societal challenges associated with their entire life cycle need to be addressed [13]. The following section outlines these aspects and describes how accurate thermal characterisation and management play a vital role in mitigating them.

The electrification of the transportation sector is a critical part of achieving global decarbonization, as EVs do not emit any tailpipe emissions [1]. However, the production of lithium-ion batteries carries a substantial environmental footprint. The mining of lithium, cobalt, and nickel, which are critical components in lithium-ion batteries, is highly energy intensive and leads to significant greenhouse gas emissions, water depletion, and ecological degradation [15]. Therefore, it is important to lower the environmental impacts by extending the operational lifetime of lithium-ion batteries.

Accurate methods for thermal characterisation provide the foundational data required to design highly efficient BTMS. Better thermal handling prevents accelerated cell degradation caused by excessive temperatures [4]. By extending the battery's lifespan, the frequency of battery replacements is reduced, thereby reducing raw material extraction [15]. In the long run, the optimisation of safer and more long-lasting batteries will accelerate the transport sector's sustainable transition to zero-emission mobility [2].

From an ethical perspective, this thesis work is firmly guided by the IEEE Code of Ethics [16]. Lithium-ion batteries are inherently susceptible to thermal runaway, which has been mentioned earlier in Chapter 1.1, can result in life-threatening fires and explosions [5].

The thermal parameters extracted from calorimetric measurements are critical for the safety design of an EV. Wrongful heat measurements or flawed characterisations can lead to the under dimensioning of the vehicle's cooling system [17]. Implementing an inadequate BTMS based on inaccurate data directly compromises vehicle safety and puts the lives of the passengers and the general public at severe risk [16]. Therefore, it is the strict ethical responsibility of the engineer to conduct these thermal experiments with high rigour, report the results honestly, and transparently disclose any experimental uncertainties or measurement errors to ensure that subsequent engineering applications are safe and reliable [16]. Moreover, the cooperative effort highlighted the importance of the second and eighth ethical codes [16]. The team's dual cultural and educational backgrounds acted as a clear advantage.

2

Theory

This chapter introduces the fundamental theory used in this work. It details the fundamental principles of heat transfer and energy balances, describes relevant heat measurement techniques and calorimeter calibration methods, and introduces the governing equations required for system modelling.

2.1 Heat transfer phenomena

The basics of heat transfer rely on three main ways that heat travels through or from a material or medium: convection, conduction and radiation. As long as a temperature difference exists, heat transfer is possible.

2.1.1 Convection

Convection is the heat transfer phenomenon where heat is exchanged between a surface and a surrounding fluid [18]. Natural convection occurs when the surrounding fluid is subject to a temperature difference. The change in density caused by the temperature difference will result in movement within the fluid, effectively moving heat away from the surface. Forced convection is when an external fan, propeller, etc., is used to control the movement of the fluid. By increasing the flow of a medium over a surface, the heat transfer increases as more fluid particles are subject to the temperature difference. For all variants of convection, the equation remains as

$$q_{conv} = h(T_s - T_\infty) \tag{2.1}$$

where q_{conv} (W/m^2) is the heat flux, h (W/m^2 K) is the convective heat transfer coefficient, and $(T_s - T_\infty)$ (K) is the difference between the surface and fluid temperature. This equation is also known as Newton's law of cooling. The heat transfer coefficient relies on the fluid and its movement. Additionally, convection can be described inside a tube or a system based on its ability to remove heat. Since the heat transfer coefficient h changes with the flow condition, the heat transfer can also be described by

$$Q_{fluid} = \dot{m} C_p (T_{outlet} - T_{inlet}) \tag{2.2}$$

where $\dot{m}$ (kg/s) is the mass flow and $C_{p,water}$ (J/kg K) is the heat capacity of the fluid . Q_{fluid} (W) is thus the resulting heat transfer from the system.

2.1.2 Conduction

Conduction is the heat transfer within materials [18]. As heated molecules move faster than cool molecules, they will collide and spread their energy to the colder molecules. The thermal energy that causes the increased molecular movement will always move from a warmer to a colder environment. Conduction follows the equation

$$q_{cond,x} = -k\frac{dT}{dx} \tag{2.3}$$

where $q_{cond,x}$ (W/m^2) is the convective heat flux in direction x. The heat flux is proportional to the temperature gradient dT/dx (K/m) in direction x. The thermal conductivity k (W/m K) is a material property and defines how efficiently heat travels through a material. The minus sign in the equation accounts for the travel from a hotter to a colder environment.

2.1.3 Radiation

Thermal radiation is the energy that is emitted by matter [18]. Radiation is highly temperature-dependent and exists for all temperatures over absolute zero. In contrast to convection, radiation does not require the presence of a fluid or medium, as it is based on electromagnetic waves (or photons). The theoretical radiation is described by blackbody radiation, but for real surfaces, relevant in this project, the emitted radiation follows the equation

$$q_{rad} = \epsilon\sigma(T_s^4 - T_{surr}^4) \tag{2.4}$$

where q_{rad} (W/m^2)is the emitted thermal radiation, ϵ is the surface emissivity, σ (Wm^{-2}K^{-4}) is the Stefan-Boltzmann constant, T_s^4 (K) is the absolute temperature of the surface and T_{surr}^4 (K) is the absolute temperature of the surroundings.

Radiation follows the principle of balance, meaning that all radiation that arrives at a surface is either reflected, absorbed or transmitted [19]. This relation can be described by

$$\alpha + \rho + \tau = 1 \tag{2.5}$$

where the absorption(α), reflection (ρ) and transmission (τ) is balanced. When a surface is at thermal equilibrium, its ability to absorb and release radiation is the same, meaning that α is equal to ϵ.

2.2 Heat & energy balance

The way that heat and energy transfers trough materials and fluids changes based on the environment. This section aims to differentiate between air and vacuum conditions and highlight the primary changes. The section will also consider relevant parameters affecting the heat balance, such as outgassing and thermal time constant.

2.2.1 Air

As heat builds up in a heat power source, it is removed through convection, conduction and radiation. The heat travelling out from the cell and cell holder can thus be written as

$$Q_{cell} = Q_{conv} + Q_{cond} + Q_{rad} \tag{2.6}$$

where Q_{conv} (W) and Q_{cond} (W) act as the main way of transporting heat. As mentioned in the previous chapter, the contribution of Q_{conv} and Q_{cond} can change drastically based on the material and fluid properties. For example, in similar conditions, water will remove far more heat than air, due to its higher heat transfer coefficient. Similarly, a metal will transfer more heat than plastic due to its thermal conductivity. In atmospheric conditions, Q_{rad} (W) acts more as a background noise, since the other heat transfer methods are far more dominant. The radiation contribution, although small, is also dependent on material properties through its emissivity.

2.2.2 Vacuum

The way that heat is transferred changes drastically in a vacuum. In a perfect vacuum, there are no fluid particles present. This means that convection is no longer possible, thus removing the primary way of transferring heat. Conduction through materials and radiation are the only ways that heat can be moved in a vacuum [18]. This changes the heat balance in a system with a heat power from a cell accordingly

$$Q_{cell} = Q_{cond} + Q_{rad} \tag{2.7}$$

Where radiation is mostly a noise factor in air, it is now the only way to transfer heat from a system without physical contact. This means that the emissivity of materials becomes far more relevant, as it dictates what absorbs and reflects radiation. In order to achieve balance in the equation, radiation has to contribute more. This means that the surface temperature has to increase, since radiation is based on $T^4_{surface} - T^4_{\infty}$ [18].

What can be considered as physical contact is different in air and vacuum. In the air, microscopic particles aid the heat transfer between two surfaces in contact.

In a vacuum, where the same particles are no longer present, the thermal contact resistance increases. This means that conduction is not as effective. This is also the reason why thermal paste or gap pads are introduced, in order to maintain sufficient contact and heat transfer.

2.2.3 Outgassing

Outgassing occurs when gas has either been trapped, dissolved, absorbed, or frozen and is being released due to the thermodynamic behaviour of gas molecules moving from a higher pressure to a lower pressure [20]. Because of this, the lowering of pressure inside a vacuum chamber will result in some degree of gas from outgassing materials into the chamber.

Though this implies that this occurs to all materials, some materials like silicone are more prone to this than, e.g. metals. The effects of outgassing often occur at higher temperatures in a vacuum. This will cause a material change to the silicone as some of its material evaporates [21]. The result of this is an effect on its thermal conductance capabilities, often resulting in the means of it being lower, as this creates small material gaps inside the material, hindering the flow of heat to pass through. As the path through the silicone becomes harder to pass through, the heat will try to seek other alternative routes to flow through instead. The effects of this ultimately result in places where outgassing thermal pads have been placed in an attempt to increase contact for thermal conduction, which will result in them performing worse than expected. The gas emitted may also condensate onto other surfaces of the setup, which can alter the equipment performance. So as to prevent unexpected and unwanted characterising changes to the setup, it can be recommended to use materials that have low outgassing [20].

2.2.4 Thermal time constant

The thermal time constant, often denoted as τ, says how fast or slow a system heats up/cools down when exposed to a change in surrounding temperature. More specifically, it represents the time for when the system has reached 63.2% of the total ΔT between its initial and final temperature [22]. As such, it's a common consideration to say that a system has reached its steady-state temperature after roughly 5τ. Determining factors behind the size of the thermal time constant, one can describe it as

$$\tau = R_t C_t = \left(\frac{L}{kA}\right)(mc_p) = \frac{\rho c_p L^2}{k} \tag{2.8}$$

where R_t (K/W) is the conductive thermal resistance and C_{th} (J/K) is the lumped thermal capacitance of the solid. In other terms, the thermal resistance states how much it resists the heat transfer, while the thermal capacitance tells how much energy the body can store.

So, the larger the system's thermal resistance and thermal capacitance are, the larger its thermal time constant becomes [22]. The result from observing a system in air and vacuum is the primary factor affecting the thermal resistance due to the difference in convective heat transfer. In the air, natural and forced heat convection help to shed heat effectively. Though in vacuum, the system only relies on conduction and radiation as the convective heat transfer is eliminated. The result of this is a significantly longer thermal time constant in vacuum than in air for the exact same system.

2.2.5 Battery

The heat profile of a battery cell can be significantly different to a simple power resistor. A battery cell can both heat and cool its surroundings, depending on the entropy profile. Entropy (ΔS) is described as the cell's disorder, quantified by the number of ways that atoms can be arranged in the crystal structure [23]. A higher entropy means more ways for the atoms to be arranged. This is crucial when determining the temperature profile of a battery, since $\Delta S < 0$ will provide heat, whilst $\Delta S > 0$ will absorb heat from the surroundings. Entropy is dependent on the state-of-charge (SOC) of the cell and is affected over time by features linked to ageing.

The heat production of a battery cell is split into two components: reversible and irreversible [23]. The irreversible heat is scaled quadratically with the current, as shown in (2.9). The reversible heat, however, scales linearly with the current as shown in (2.10), and is therefore more present at lower C-rates.

$$Q_{irreversible} = I^2 R \tag{2.9}$$

$$Q_{reversible} = IT \, \frac{dE_{ocv}}{dT} \tag{2.10}$$

where I (A) denotes the current, R (Ω) the internal resistance, T (K) the absolute temperature and dE_{ocv}/dT (V/K) is the entropic coefficient which is directly linked to ΔS (J/mol K) trough Gibbs energy, following

$$\Delta S = nF \, \frac{dE_{ocv}}{dT} \tag{2.11}$$

2.3 Heat measurement techniques

Heat is often considered a waste of energy and an unwanted reaction for many applications. Successfully measuring the heat can be crucial for understanding and improving the system.

2.3.1 Calorimeter

The purpose of a calorimeter is to measure heat. In this report, an isothermal approach is used, where conduction leads the heat through heat flow sensors. In its simplest form, the calorimeter requires three parts:

- **Heat source** with a known heat power provides a baseline for the recorded heat flow.
- **Heat flow sensors** detect the temperature change between their hot and cold sides.
- **Heat sink** maintains a constant temperature on the opposing side of the heat flow sensor and allows for a steady temperature difference.

In the experiments conducted in this report, Peltier elements were chosen as heat flow sensors. These elements work on the principle of the Seebeck effect, where a temperature difference across an electrically conducting material creates an electromotive force [24]. In a Peltier element, Bismuth Telluride (Bi_2Te_3) is used as n-type and p-type materials, creating a thermocouple. When a temperature difference is applied to the doped materials, a voltage signal is created that is proportional to the temperature difference [25]. The Seebeck coefficient (α) is described as

$$\alpha = \frac{U}{\Delta T} \tag{2.12}$$

where U (V) is the Seebeck voltage created and ΔT (K) is the temperature difference over the thermocouples. A Peltier element is composed of multiple thermocouples that are electrically connected in series and thermally connected in parallel. Ceramic plates are used on both sides of the thermocouple junction to electrically insulate the element [24].

Depending on the degree of quality required in the measurements, isolating the setup might be needed. This limits the spread of heat in unwanted directions and forces it through the heat flow sensors for better measurements. Similar experiments have seen the use of styrofoam [26], or glass wool [17]. The goal of this project is to investigate the use of a vacuum as an insulator.

2.3.2 Cooling

Vacuum and air both require effective cooling to maintain a steady cold side reference for the calorimeter. To achieve cooling, the implementation of water-cooled heat sinks is used, where the heat travels by conduction from the heat source to the heat sinks. The circulating cold water will then capture the heat and remove it from the system, keeping the system at a relatively constant temperature. To achieve as much

heat transfer by the circulating water as possible, it is preferable to have a turbulent water flow circulating instead of a laminar one. The reason is that the eddies cause intense mixing of the water, making it more effective for absorbing heat [27]. To know if a turbulent water flow is present, the Reynolds number is considered, which for a circular pipe is

$$Re = \frac{\rho v D}{\mu} \tag{2.13}$$

where ρ (kg/m^3)is the liquid density, v (m/s) is the average velocity of the liquid, D (m) is the diameter of the pipe, and μ (Pa $\cdot$ s) is the dynamic viscosity of the liquid. From the equation, it can be determined that the flow is turbulent if $Re > 4\ 000$ [27]. Though in some cases the heat sinks have semicircular pipes through which the water circulates within the heat sink. For these cases, the diameter is swished out with the hydraulic diameter D_h (m), which is described as

$$D_h = \frac{4A}{P} = \frac{\pi D}{\pi + 2} \tag{2.14}$$

where A (m^2) is the cross-sectional area of the semicircle, P (m)is the wetted perimeter, and D (m) is the straight diameter of the semicircle.

2.4 Calorimeter calibration

Peltier elements and the Seebeck coefficient can also be assessed by the material properties. Based on data from the supplier, the Seebeck coefficient (α) for one peltier element is given in (2.15) and (2.16). The coefficient is found for the n- and p-legs thermoelectric material, Bi_2Te_3. Note that the material properties are temperature-dependent, although this dependence is mostly relevant at more extreme temperatures.

$$\alpha_n(T) = (0.001530736T^2 - 1.08058874T - 28.338095) \times 10^{-6}\ [\text{V/K}] \tag{2.15}$$
$$\alpha_p(T) = (-0.003638095T^2 + 2.74380952T - 296.214286) \times 10^{-6}\ [\text{V/K}] \tag{2.16}$$

Similarly, the thermal conductivity, k, is calculated from (2.17) and (2.18).

$$k_n(T) = 0.0000334545T^2 - 0.023350303T + 5.606333\ [\text{W/mK}] \tag{2.17}$$
$$k_p(T) = 0.0000361558T^2 - 0.026351342T + 6.22162\ [\text{W/mK}] \tag{2.18}$$

It is important to note that the T (K) implied in (2.15)-(2.18) is the mean temperature of the Peltier materials. This is not to be confused with the temperature difference used when assessing the voltage output of the elements.

For each peltier element, the following is applied for finding the Seebeck coefficient, S_{Module} (V/K), and thermal conductivity, K_{Module} (W/K), for one peltier module

$$S_{Module} = N(\alpha_p - \alpha_n) \tag{2.19}$$

$$K_{Module} = N(k_n - k_p)\frac{A_{tc}}{L_{tc}} \tag{2.20}$$

where N is the number of thermocouples, set at 127 for the GMS250-127 elements, A_{tc} (m^2) is the cross-sectional area of each thermocouple at 1.6 mm^2, and L_{tc} (m) is the height, being 1.0 mm.

The calorimeter is assembled so that two Peltier elements are connected electrically in series on each side of their respective sample. As the heat will travel symmetrically towards both heat sinks A and B, the Peltier elements are considered as a thermal parallel coupling. With two Peltier elements on each side, this means

$$S_{system} = 4S_{Module} \tag{2.21}$$

$$K_{system} = 4K_{Module} \tag{2.22}$$

In order to transform the recorded Peltier voltage into a heat power, a calibration coefficient (ϵ) is used. The calibration coefficient exists in both theoretical and experimental forms. The theoretical calibration coefficient is described by the Peltier elements' material properties, following

$$\epsilon_{theoretical} = \frac{K_{Module}}{S_{Module}} = \frac{K_{system}}{S_{system}} \tag{2.23}$$

The experimental version is the relation between the heat travelling through the sensor, or in this instance, supplied by the dummy cell, and the voltage recorded from the Peltier elements. A calorimeter can be calibrated with two methods, steady state and the pulse method. As described by *Wadso* (2010, [28]), the methods differ by only 0.12%. This project utilised the steady-state calibration method, which requires the system to reach a constant thermal plateau. The calibration coefficient (ϵ) is calculated using the following relationship,

$$\epsilon_{experimental} = \frac{P}{\Delta U} \tag{2.24}$$

where P is the supplied power from the dummy cell, and ΔU is the voltage difference recorded by the Peltier elements at the dummy cell and the reference object.

For the experimental calibration coefficient, it can be used together with the theoretical one to calculate the measured heat flow ratio (MHFR)

$$MHFR = \frac{\dot{Q}_{out}}{\dot{Q}_{in}} = \frac{\epsilon_{theoretical}}{\epsilon_{experimental}} \tag{2.25}$$

where MHFR is the percentage of the measured heat, $\dot{Q}_{out}$ (W), being compared against the total input heat $\dot{Q}_{in}$ (W). This relationship works as the voltage signal is directly proportional to the heat captured. Therefore, the MHFR is the ratio of the theoretical calibration coefficient to the experimental calibration coefficient.

As an alternative to the steady-state approach, pulse calibration involves applying a known thermal power (P) for a short, defined duration (Δt). Rather than waiting for a thermal plateau to form, the calibration coefficient is determined by integrating the baseline-corrected voltage signal (U) over the entire duration of the heat pulse

$$\epsilon_{experimental} = \frac{P\Delta t}{\int U dt} \tag{2.26}$$

A key theoretical advantage of this integral approach is derived from the Tian-Calvet equation, which describes the instantaneous dynamic thermal power of a calorimeter,

$$P(t) = \epsilon \left[U(t) + \tau \left(\frac{dU}{dt} \right) \right] \tag{2.27}$$

where τ is the thermal time constant of the system. By integrating the signal from the start of the pulse until the system fully returns to thermal equilibrium, the dynamic derivative term mathematically integrates to zero. Consequently, the total energy of the pulse can be perfectly extracted without needing to determine the system's dynamic time constant [17].

Despite its potential to significantly reduce the time spent waiting for thermal equilibrium, pulse calibration has distinct limitations. It requires the precise recording and integration of the entire thermal decay, often referred to as the cooling tail [17]. If the system experiences baseline drift during this extended decay period, the integrated area will be skewed, leading to calibration errors [28].

The use of a reference sample is crucial to achieving successful measurements from a calorimeter [28]. By placing a reference sample in the same calorimetric setup as the test sample, the recorded voltages can be compared to the baseline set by the reference sample. The reference is used to simulate the test sample in identical conditions, just without the heat source. Thus, it is important that the reference sample is of the same material and physical properties as the test sample. The use of a reference sample is a great addition to remove noise and ambient effects from the experimental data.

3

Case setup

This chapter will explain and show how the experimental laboratory testing has been conducted. An overview of the setup, CAD model and sensor placement will also be featured. Key figures for the testing equipment will be presented to explain its limits and accuracy. The chapter will also explain how the testing setup has been developed and changed throughout the project, along with the motivation for the changes. As part of the calibration of the calorimeter, several calibration tests have been performed on the sensors and equipment. At last, the development of the digital-twin model is explained and motivated with assumptions.

3.1 Initial setup

Conducted experiments were done on the setup simplified in Figure 3.1. The setup utilises a vacuum chamber of size 500 mm × 500 mm × 500 mm that accommodates a custom-built calorimeter. The calorimeter is placed on a 3D-printed stand and is divided into sides A and B.

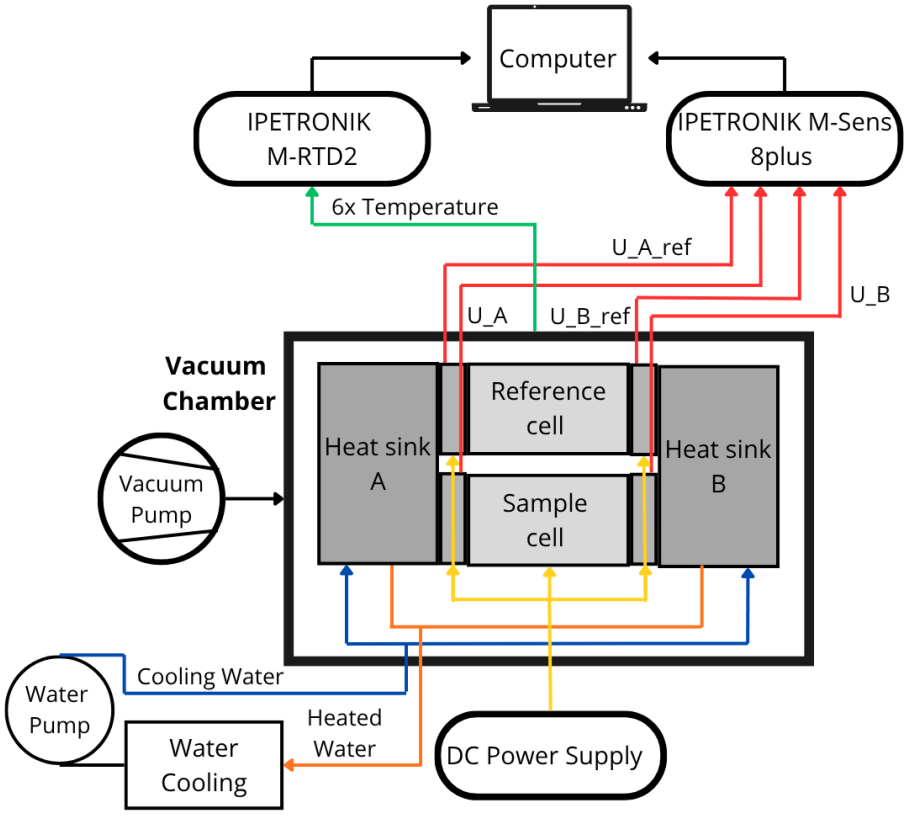

Figure 3.1: Schematic drawing of the experimental setup

Outside the vacuum chamber is a combined liquid cooling and pumping system, Julabo Corio, supplying liquid cooling, a DC power unit, Keysight EDU36311A, supplying power, and a vacuum pump, HiScroll 12, lowering the pressure inside the vacuum chamber. Temperature is measured using PT100 temperature sensors, and through Peltier elements, the heat flow is measured as an output voltage. Figure 3.2 showcases in more detail how the calorimeter is set up. In between heat-sinks A and B are the Peltier elements, which are connected two-by-two in series for both sample and reference on each side, making a total of 8 Peltier elements of 4 pairs. The sample and the reference side have both a cylindrically-hollow 73 mm $\times$ 73 mm $\times$ 93 mm aluminium block, which allows the cylindrical sample cell to achieve contact with the Peltier elements.

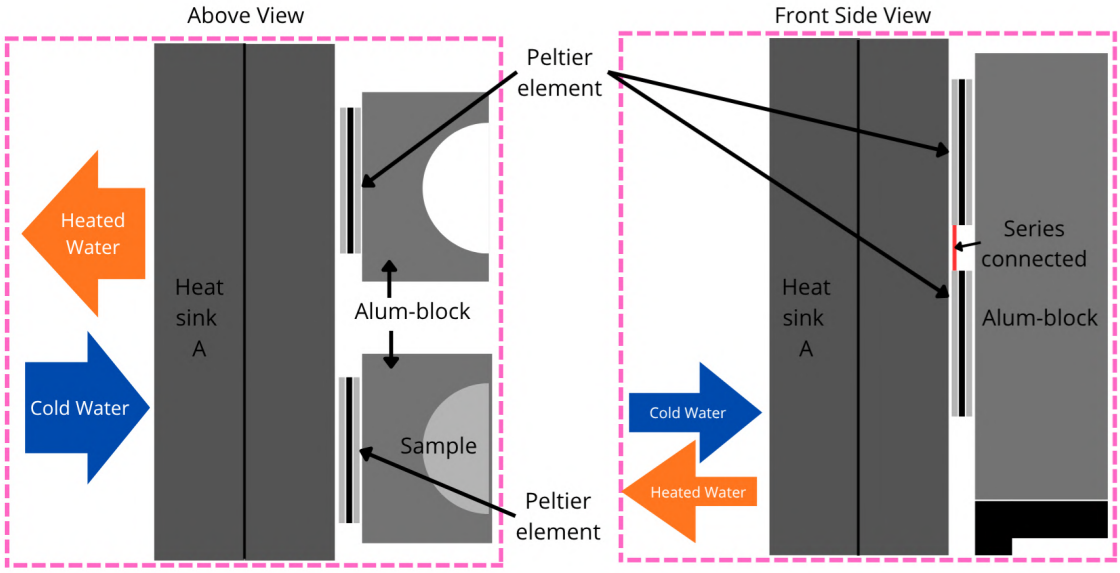

Figure 3.2: Calorimeter setup seen from above and the side

The assembly of the calorimetric setup was performed by the authors together with the supervisor. The heat sinks, which are two aluminium blocks put together, are mounted together with screws, creating a sealed tube for the cooling liquid. This is because the outer block on each heat sink has a semicircular score for the cooling liquid to flow through. Figure 3.3 shows an illustration of how the water flows inside each heat sink.

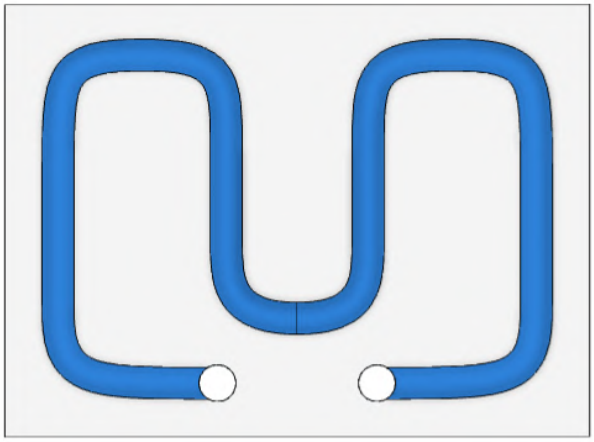

Figure 3.3: Illustration of the heat sink's internal path

From the figure, it can be seen that the liquid flows in from one hole at the bottom, then through the heat sink in an M-shape, and then out again through the other bottom hole. As the heat sinks had been used in prior experiments, the old Peltier

elements and thermal sheets were removed before new elements could be mounted. In order to achieve proper thermal contact between the Peltier elements, the heat sink and the core, a thermal gap pad is applied.

Throughout the project, two distinct types of thermal gap pads were used. First, they were silicone-based and were used during the start of the project. The specific ones used were the RS Pro GCSP-28 Self-Adhesive Thermal Gap pads, which have a thickness of 0.5 mm and a thermal conductivity of 2.8 W/mK. The second type used during the other part of the project was acrylic-based. These were the Bergquist Self-Adhesive Thermal Interface Pad CPU pad, which has a thickness of 0.127 mm and a thermal conductivity of 0.6 W/mK. The two thermal pads are both adhesive, which was a requirement to be able to mount the Peltier elements. Figure 3.4 shows what they look like mounted onto the heat sink.

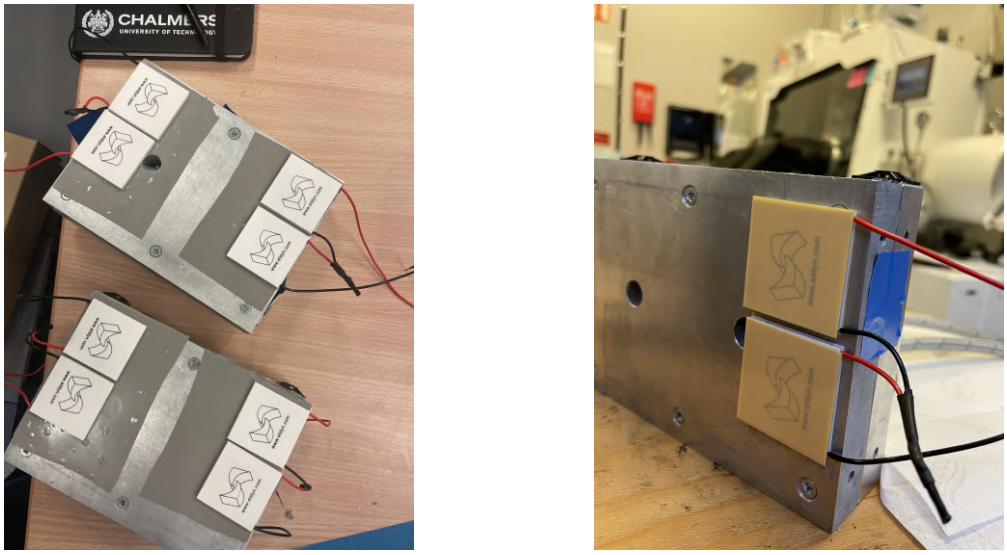

(a) Silicone-based **(b)** Acrylic-based

Figure 3.4: Thermal gap pad on Peltier elements for the various stages

The dummy cell and its holder were lined up with one column of Peltier elements on each heat sink. An aluminium block, identical to the one holding the dummy cell, is placed on the opposing column of Peltier elements, acting as a reference cell. With everything positioned, the setup is held together by clamps on each side. The compression from the clamps also improves the thermal contact for the Peltier elements. The assembled setup can be seen in Figure 3.5, where it is placed in the vacuum chamber and connected to sensors, power and liquid cooling.

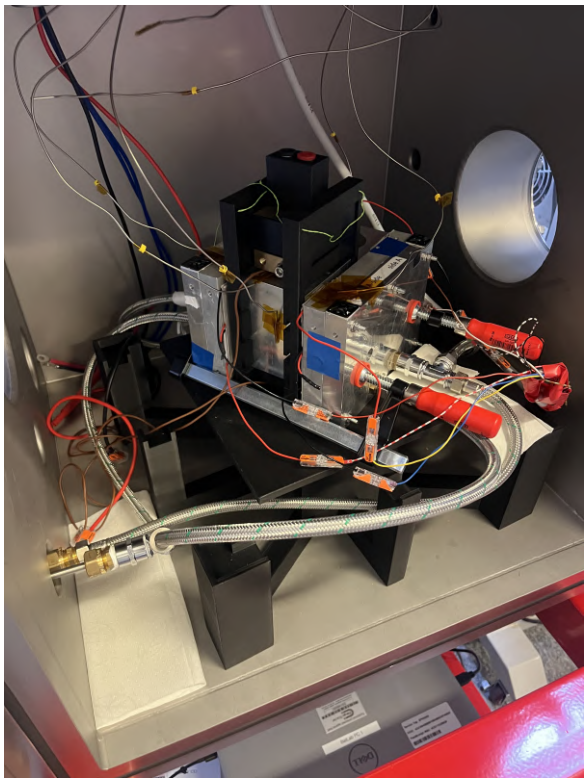

Figure 3.5: Calorimetric setup with dummy cell in vacuum chamber

As seen in Figure 3.5, a T-connection is used for the cooling liquid. This allows the heat sinks to be connected in parallel, providing symmetrical cooling for the cell. On the outside of the vacuum chamber, the tubes are connected to a Julabo Corio CD-200F refrigerated/heating circulator. This unit is filled with distilled water, which acts as the cooling liquid for the setup. Furthermore, the placement of a total of 6 PT100 temperature sensors can be spotted in Figure 3.5. Figure 3.6 shows the exact placement better with two sensors placed on the sample (C and D), two placed on top of each heat-sink (A and E), one on the reference (B), and the last one is placed above the calorimeter hanging freely inside the vacuum chamber to monitor the air temperature.

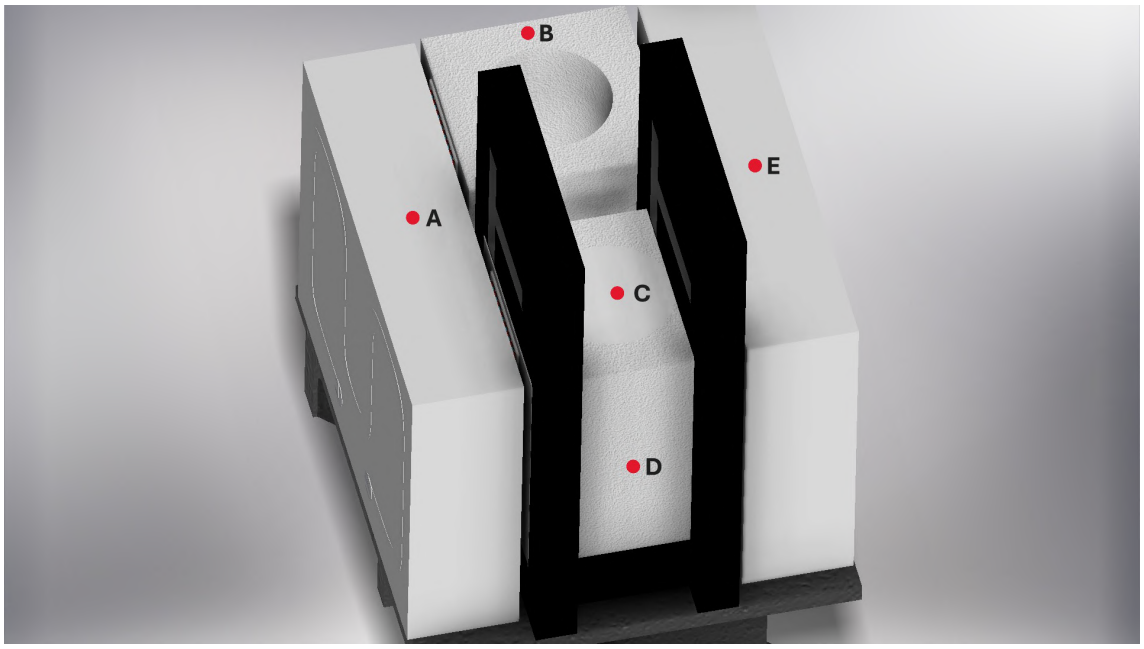

Figure 3.6: PT100 temperature sensor placement showing 5 of 6 sensors used

3.2 Measurement equipment

Quality measurement equipment is vital for ensuring the data quality of the experimental tests. For the laboratory work of this thesis, the battery lab at Chalmers University of Technology is used. As this lab is used for research on batteries, it allows for the use of high quality equpiment. Table 3.1 gives a summary of the relevant technical data of the measurement equipment. A Keysight EDU36311A power supply is used for accurate voltage and current delivery. This unit is connected to the dummy cell directly through channel 3. Channel 2 is used to supply power to the M-SENS 8plus voltage module, which measures the voltage output of the Peltier elements. Channel 2 is also connected to two M-RTD2 temperature modules that are used to measure the temperature at various positions in the vacuum chamber. [29, 30, 31]

Table 3.1: Measuring equipment and test load

M-SENS 8plus (voltage module)	
Measurement range	±10 mV up to ±100 V ±20 mA
Accuracy at ambient temp (25°C)	±0.06% (bipolar) ±0.10% (unipolar)
Channels	8
AD converter	16 bit / SAR

M-RTD2 (temperature module)	
Measurement range	−50 to 450°C
AD converter	16 bit / SAR
Accuracy at ambient temp (25°C)	±0.020% for full range (±0.1°C calculated)
Theoretical resolution	0.0076°C (16-bit)

Keysight EDU36311A (power supply)	
Channel 1	0–6 V, 0–5 A
Programming accuracy (C1)	0.1% + 5 mV 0.1% + 10 mA
Channel 2 & 3	0–30 V, 0–1 A
Programming accuracy (C2 & 3)	0.05% + 10 mV 0.2% + 5 mA
Output ripple (normal mode)	< 1 mVrms / 5 mVpp < 4 mArms

The dummy cell is placed in the core of the test setup. This cell uses an Arcol HS100 resistor as a heat source. The ability to have a constant known heat source proved important for the calibration of the setup. The resistor is stripped of its standard heat sink and placed in the aluminium core. Although the power rating without a heat sink is reduced to 30W, the resistor will be run at a max power of 5W, well within its safety limits. Table 3.2 shows a technical summary of the resistor. [32]

Table 3.2: Technical data for the dummy cell resistor

Arcol HS100 (resistor)	
Resistance	15 Ω
Power rating w/ heat sink (at 25 °C)	100 W
Power rating wo/ heat sink (at 25 °C)	30 W
Temperature coef. (TCR)	± 100 ppm/°C
Max surface temperature	200 °C

The Peltier elements are a key component in the calorimeter setup, as it allows for the measurement of a voltage as a response to the temperature difference. To ensure quality measurements, new Peltier elements are applied in the setup. Table 3.3 shows the technical data of the new Peltier elements. [33]

Table 3.3: Peltier Module Specifications

Adaptive GM250-127-14-10	
Dimensions ($A \times B \times H$)	$40 \times 40 \times 3.4$ mm
Max operation temp (Hot side)	250°C
Matched load output power	9.9 W
Matched load resistance	$2.49\ \Omega \pm 15\%$
Open circuit voltage	9.93 V
Maximum compression	1.2 MPa

In order to keep the setup at a steady temperature, a heating circulator is connected to the heat sinks. The pump must be able to provide enough cooling to keep the heat sinks at a near constant temperature. With 220 W of cooling capacity and a flow rate of 15 L/min, the CORIO CD-200F in Table 3.4 delivers constant operation. [34]

Table 3.4: Specifications for the cooling pump/bath

JULABO CORIO CD-200F	
Working temperature range	−20 to +150°C
Temperature stability	±0.03°C
Heating capacity	2 kW (at 230V) / 1 kW (at 115V)
Cooling capacity (at 20°C)	0.22 kW
Pump capacity (flow rate)	15 l/min
Pump capacity (flow pressure)	0.35 bar (5.1 psi)

3.3 System validation

In order to verify that the results are trustworthy, a sensor/equipment quality check is performed. The goal of this check is to see if there are any significant inaccuracies or sources of error. As vacuum is the main topic of interest for this report, the calibration tests are primarily performed in a vacuum. The sensor calibration was a part of the two-stage testing, where various changes were made to the setup underway to explore their effects. All of the calibration tests (stage II-IV) are done with the acrylic thermal gap pads.

Table 3.5: Stages of development for system calibration

Stage	**Name**	**Core components**	**Purpose**
I	Preliminary testing	Si-based thermal pads No isolation Reference cell	Initial characterization of ϵ
II	Material exploration	Acrylic thermal pads No isolation No reference cell	Minimise thermal contact resistance Limit silicone outgassing
III	Thermal optimization	Acrylic thermal pads External isolation Reference cell 15°C cooling	Isolate chamber Sensor calibration
IV	Final configuration	Acrylic thermal pads External & internal isolation Reference cell 15°C/25°C/35°C cooling	Isolate chamber/setup Final sensor calibration

All previous testing had been done using 25°C water as coolant for the heat sinks. The temperature of the water was then changed to 15°C for the stage III and IV tests. Stage IV was ultimately run at 15°C, 25°C and 35°C, in both air and vacuum. This was done to observe how the system behaved in a different environment where the surrounding (lab) temperature would be significantly different from the temperature of the setup. It would also reveal the cooling capacity of the heat sinks and how a lower temperature would affect the chamber.

3.3.1 Temperature sensor

The calibration of the PT100 temperature sensors is done in two stages in order to test various applications of the sensors. One test is performed to test the sensors

themselves. This includes leaving the sensors in free space. This will explore if the sensors show the same temperature and are thus calibrated correctly. AA class sensors have an accuracy of $\pm(0.1 + 0.0017|T|)°C$ and are known as highly accurate temperature sensors [35]. The setup used is shown in Figure 3.7a. The test is run without any applied heat.

The second calibration test is performed by attaching all PT100 sensors to the same heat sink. The goal of this test is to explore the sensor's connection to the materials in the setup. When testing in the air, convection helps overcome tiny gaps between the sensors and the setup. In a vacuum, sufficient thermal contact will be crucial to achieving accurate measurements. The test will run without any applied heat power, which means that uniform heat dissipation within the heat sink is assumed. The duration of the tests is dictated by the time constant of 4 hours for a vacuum. The setup for this test is shown in Figure 3.7b.

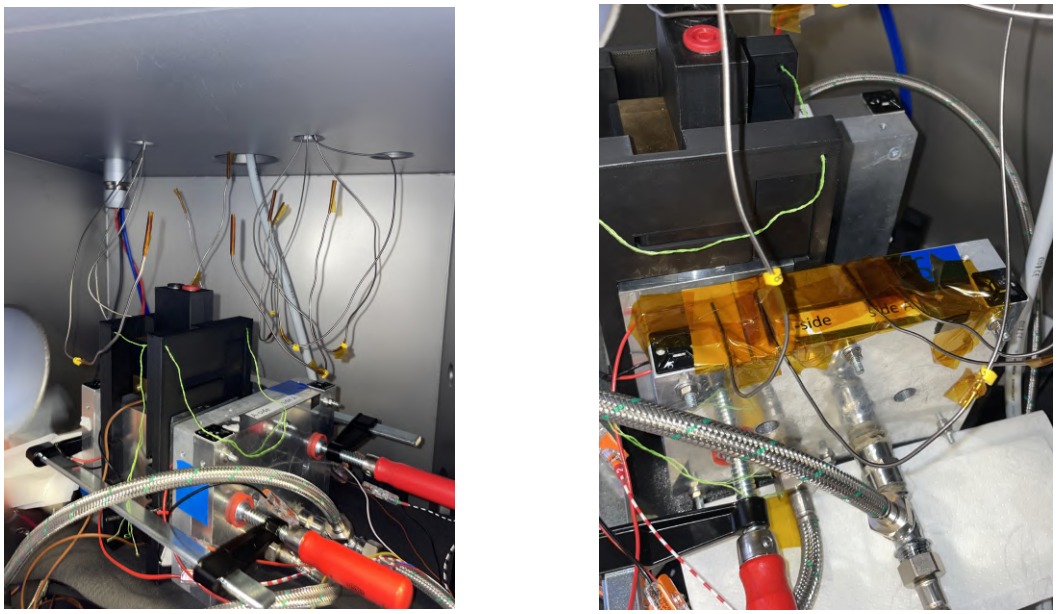

(a) Stage IV **(b)** Stage III

Figure 3.7: Calibration of PT100 sensors during stage III and IV

As mentioned, the second calibration test was aimed at exploring the sensors' connection to the setup. The sensors are attached using Kapton tape, which is electrically insulating and suited for a large range of temperatures. However, the stiffness of the sensors proved to be a problem for the adhesive capability of the tape, which inspired this test. The goal of the test was therefore to see what combinations of tape and thermal gap pad would give the best connection. To explore conduction from the cables to the setup, two sensors were placed without any isolating tape around them. Various connections were thus tried:

- **Sensor 1** No isolating tape. No thermal gap pad.
- **Sensor 2** Isolating tape. No thermal gap pad.

- **Sensor 3** No isolating tape. Thermal gap pad.
- **Sensor 4** Isolating tape. Thermal gap pad.

3.3.2 Peltier elements

The most crucial part of the setup is the heat flow sensors. To ensure that the Peltier elements work as intended, two tests were performed. The first test included placing an identical element loose in the setup while running other tests. It was assumed that each sensor performed identically, as individual verification of each sensor would be time-consuming. The second test was aimed at exploring the residual heat in the setup. The calorimeter was opened, and the sensors were left with one side exposed. As the adhesive properties of the new thermal gap pads were significantly higher than the previous ones, removing the Peltier elements proved challenging. Therefore, the elements on heat sink B remained attached, whilst the elements on heat sink A stuck to the sample and reference. In theory, the non-existent convection from the vacuum should prevent heat transfer through the Peltier elements. No applied heat was used for this test, although the cooling remained on. The setup for both tests is shown in Figure 3.8.

(a) Stage II **(b)** Stage III

Figure 3.8: Calibration of Peltier elements in stage II and III

3.3.3 Isolation

Properly isolating a calorimeter is crucial for its accuracy and function. Although vacuum should be an excellent isolator, a perfect vacuum is hard to achieve. Therefore, various tests were done to see if any heat sources affect the calorimeter setup and its measurements.

The first step involved attaching temperature sensors to the roof of the vacuum

chamber and to the 3D-printed stand, as shown in Figure 3.9. Since the tests were not performed in a perfect vacuum, some convection heat transfer is still present. Combined with radiation, the chamber walls are also subject to heat transfer, which will affect the measurements.

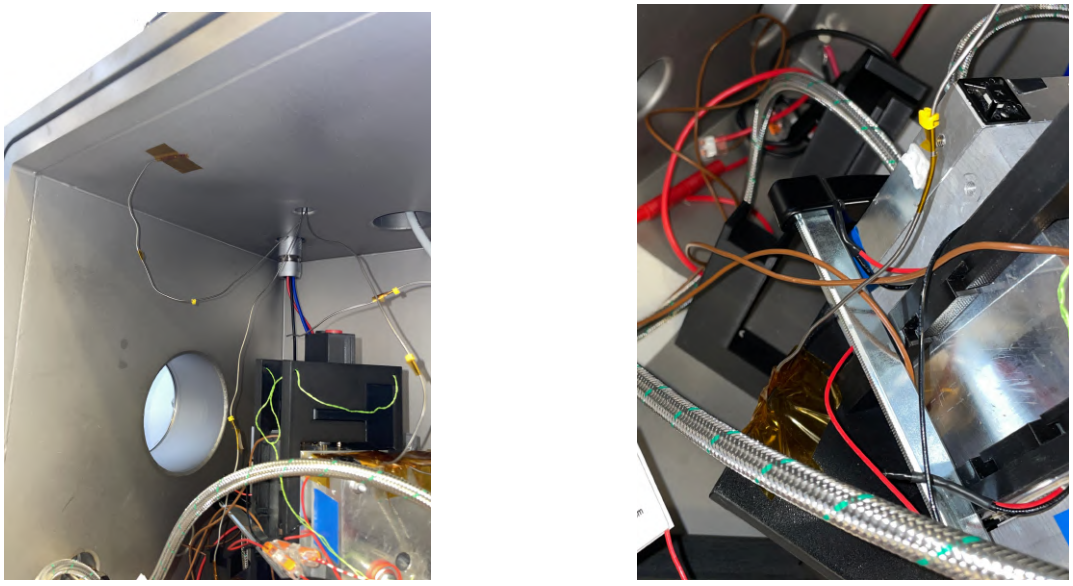

(a) Vacuum chamber roof **(b)** 3D printed stand

Figure 3.9: Placement of temperature sensors in chamber at stage III

An attempt to isolate the outside of the chamber was made. This test is done to see how the connected units affect the temperature of the chamber. The primary suspects were the vacuum pump placed under the chamber and the sensor modules placed directly on top of the chamber. The isolation is shown in Figure 3.10.

(a) Vacuum pump **(b)** Modules

Figure 3.10: Thermal isolation against the vacuum pump and the temperature/voltage modules

In stage IV, internal isolation was also added. This was done to see if there was any heat transfer from the chamber to the base of the stand, and from the stand to the calorimeter. The placement of the isolation is shown in Figure 3.11.

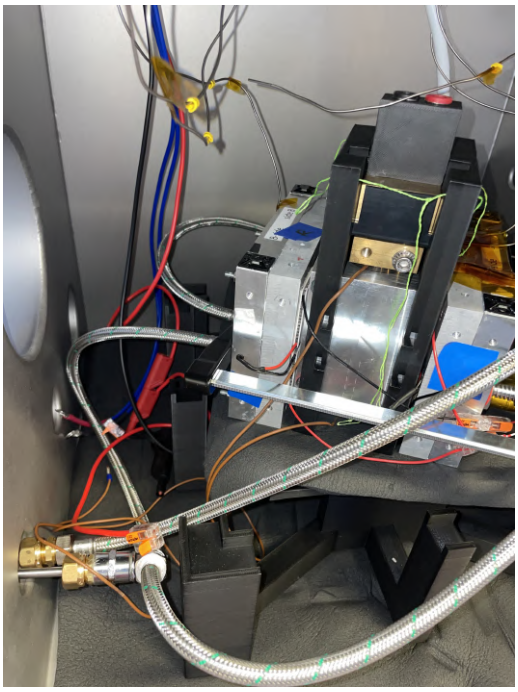

Figure 3.11: Isolation inside vacuum chamber in stage IV

3.3.4 Cooling system

The Julabo cooling system is rated for 15 L/min and 220 W of cooling. As the flow rate is dependant in the pressure, a test was performed to verify the flow rate of the cooling system. The test was performed by manually measuring the flow rate. The idea was to run the cooling system with the outlet hose in a separate bath. By measuring the time and volume, the flow rate could be calculated. For simplicity, the test was supposed to run for 60 s and then read the measured volume. However, as the pump emptied the bath reservoir faster than it could be manually filled, the system stopped after about 10 s with an error message. This resulted in the experiments being run for only 5-10s and then using the measured values to calculate the flow rate in L/min. Figure 3.12 shows the setup used for the flow rate test

Figure 3.12: Flow rate test

3.4 Physics-based model

To validate and further prove the experimental results, a physics-based model was simulated in COMSOL Multiphysics. Although no simulation can perfectly replicate reality, computational models remain invaluable tools for estimating outcomes and predicting system behaviour. As George E. P. Box famously remarked, "All models are wrong, but some are useful" ([36]).

3.4.1 Computational model

For this project, a 3D CAD model was built in the software Autodesk Inventor. Computational cost and accurate geometry were considered in the final design showcased in Figure 3.13. The model was used for both air and vacuum.

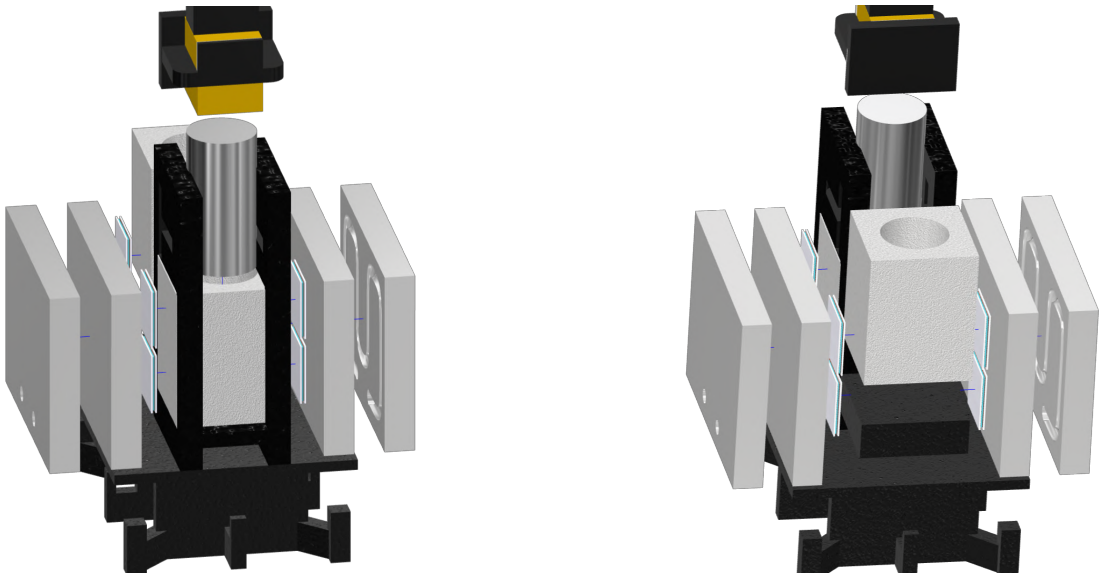

(a) Front **(b)** Back

Figure 3.13: Exploded view of the calorimeter CAD assembly

For the modelling of the vacuum chamber, a 500 mm × 500 mm × 500 mm hollow cube with a wall thickness of 20 mm is used. Although it was desired to replicate the physical model as closely as possible, ideas such as modelling the water tubes around the setup were scrapped to maintain a reasonable computational time. Another concept that was tested was modelling the Peltier elements with great detail, as shown in 3.14a, where the pellets and bridges of the elements are included. Similarly, this became too heavy and time-consuming for efficient simulation and was therefore replaced with plates instead of pellets, as shown in Figure 3.14b.

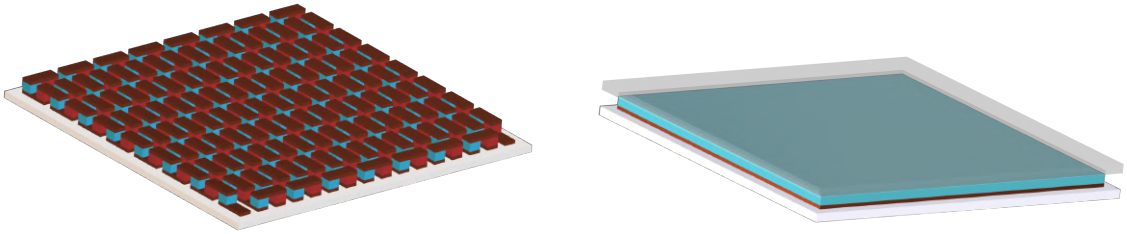

(a) Detailed 3D CAD model **(b)** Simplified 3D CAD model

Figure 3.14: 3D CAD models for Peltier element GM250-127-14-10

The CAD model was imported into COMSOL Multiphysics, and the components were assigned to the materials shown in Table 3.6. Assumptions were made, especially for the dummy cell, to better replicate the results from the physical setup. The Peltier elements are assumed to be Bi_2Te_3, commonly used in Peltier elements and thermoelectric modules [37].

Table 3.6: Thermal and electrical properties of materials.

Modules	**Material**	ρ [kg/m^3]	C_p [J/(kg K)]	k [W/(m K)]	ε	σ [S/m]	μ [Pa s]
Alum. block, Heat sink, Chamber	Aluminium	2700	900	238	0.05 0.15 0.95	N/A	N/A
Dummy cell	Lumped materials	3000	850	20	0.05	9.38	N/A
Electrical components	Copper	8960	385	400	0.04	6.00×10^7	N/A
	Gold	19320	130	320	0.02	4.1×10^7	N/A
	Rubber	1100	1900	0.5	0.95	N/A	N/A
	Plastic	1300	1270	0.18	0.94	N/A	N/A
Liquid cooling	Water	998	4184	0.6	N/A	N/A	8.9×10^{-4}
Peltier elements	Ceramic	3220	419	31	0.85	N/A	N/A
	Copper	8960	385	400	0.65	N/A	N/A
	Bi_2Te_3	7740	200	0.496	0.50	N/A	N/A
Stand, Sample holder, Ref. holder	Plastic	1300	1270	0.18	0.94	N/A	N/A

3.4.2 Physics & boundary conditions

For the physics to more accurately capture the thermal response of the calorimeter, governing equations and multiphysics couplings specific to heat transfer, turbulent flow, and electric current are used. The specific ones used for both the air and vacuum models are detailed and found in Appendix A.3. The initial conditions and BCs are chosen to the best of the model's ability to replicate the underlying conditions.

Looking at the conditions set for the turbulent cooling liquid, its initial properties are set to the material properties listed in Table 3.6 and a starting temperature. The inlet velocity of water at the heat sink is set to 6.63 m/s and is an estimated value based on the tested pump capacity, which is mentioned in Chapter 3.3.4. For the internal walls inside heat sinks where the fluid flows, a no-slip boundary condition is also applied, stating that the velocity of the fluid against the solid-fluid interface is zero due to viscous effects.

To compensate for the geometric simplification set for Peltier elements previously stated and seen in Figure 3.14, a solid BC is put on the Bi_2Te_3 material and the copper inside the Peltier element. It constrains the thermal conductivity to the through-plane direction, effectively eliminating transverse heat conduction. Furthermore, both thermal conductivities for Bi_2Te_3 and copper are also lowered by 64.4% and 51.7%, respectively.

The effects of the thermal pads set on both sides of each individual Peltier element are simulated utilising a thin-layer BC. It tells the model to envision the existence

of thermal pads of specific thickness and material properties. As the acrylic thermal pads were used for most of the experiments, the parameters for them are utilised in the BC. These specific values, retrieved from the data sheet and general intuition based on the material, are found in Table 3.7.

Table 3.7: Thermal pad data for thin-layer BC

Acrylic pad variables		**Values**
$L_{thickness}$	[mm]	0.127
ρ	[kg/m^3]	1200
C_p	[J/(kg K)]	1400
k	[W/(m K)]	0.6

For the specific BCs needed for simulating the different cooling paths occurring at atmospheric and vacuum conditions, different conditions were set at the exterior surfaces of the model as a result of the environment in itself not being modelled. The air model simulates natural convection conditions, with a convective heat transfer coefficient at 5.0 W/m^{2}K assuming normal conditions. It also takes surface-to-ambient radiation into consideration with set surface emissivity values stated in Table 3.6.

In the simulation of a vacuum environment, the convective cooling is completely disabled. Instead, dissipation of heat to its surroundings is entirely assumed to be surface-to-surface radiation. For this, the same surface emissivity values stated in Table 3.6 are used.

Lastly, the heat generated by the power resistor is defined by BCs within the Electric Currents interface. A specific electrical terminal was defined at one end of the circuit to apply the variable current based on the desired power level (e.g., 0.5 W, 1 W, 5 W), while the opposite end was set as the electrical ground (U = 0 V).

3.4.3 Numerical methods

To improve computational efficiency, it was decided to cut the geometry in half, as seen in Figure 3.15a. Decreasing the geometry for which to solve the numerical solutions results in fewer mesh elements and so lowers the computational cost of the model regarding both memory and time.

The geometry is then meshed in accordance with the relative size of the different domains. For example, the chamber walls are set with a coarser element sizing, while the Peltier elements utilise a finer mesh as they are both smaller in size and require a high accuracy for the heat flow analysis. The final mesh for computational solutions has 238 625 numbers of elements with an average element skewness quality

of 0.65, which can be seen as good for the physics simulations wanting to evaluate. This mesh quality can further be seen in Figure 3.15b.

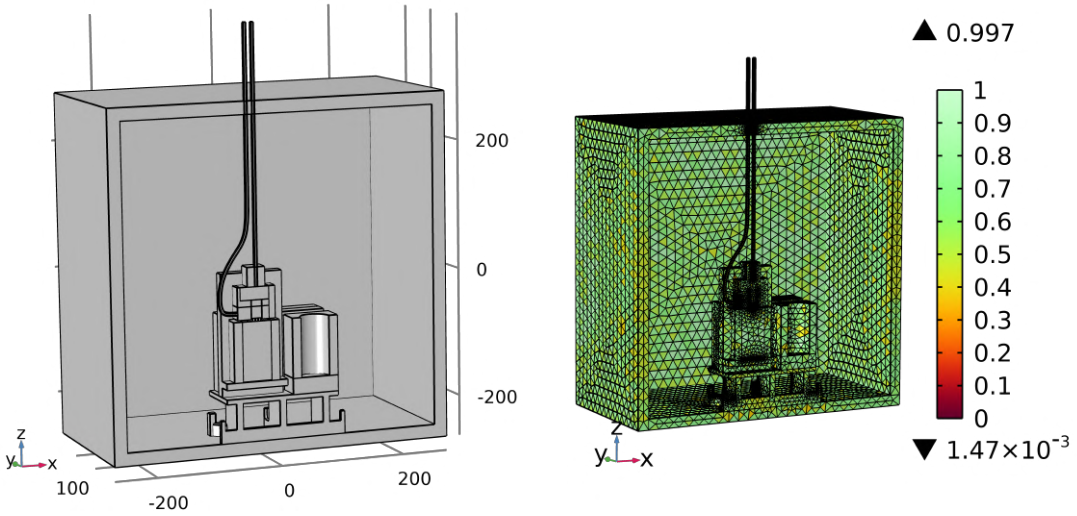

(a) Split geometry, sizing in millimetres **(b)** Mesh skewness over the geometry

Figure 3.15: Physics-based split geometry and its applied mesh

Seen in Figure 3.15, the lowest skewness quality is at 1.47E-3, which can be considered to be bad. After looking into the number of elements with bad quality (skewness < 0.1), it was concluded that,t these were few. For that reason, this was overlooked so as not to make the simulation computationally costly.

For the simulation data, both time-dependent and stationary solvers were utilised. The Boussinesq approximation is used for the circulating cooling liquid and its turbulence variables. These values, along with the electric current, are solved stationarily prior to the time analysis. Additionally, appropriate initial values for the temperature of the sample cell are found using a stationary solver. The solved stationary solutions are used as the initial starting condition for the time-dependent solver, which solves for the heat transfer and radiation. The end times for which the simulations are solved are predicted based on experimental data from the calorimeter setup and iterative work, with the finishing simulated time intervals being 2 hours for the air simulation and 4 hours for the vacuum simulation, with 1 min and 2 min time stepping, respectively.

3.4.4 Model modification on experimental data

As one goal of the thesis was to make the physics-based model as good a digital twin as possible, the collected data was used as a benchmark for the simulation. Three main changes proved necessary in order to best replicate the physical setup, as shown in Table 3.8. The changes are made to the conductive heat transfer coefficient of the Peltier elements, the heat capacity of the sample cell and the temperature of

the water inlet. It is worth noting that the changes are made primarily to replicate the behaviour of the physical setup, not to speculate on the physical properties.

Table 3.8: Modified parameters for physics-based model

Variables	**Original values**	**Air**	**Vacuum**
$k_{thermal\ pad}$ [W/(m^{2}K)]	0.6	0.36 (- 40%)	0.06 (- 90%)
$C_{p,\ dummy\ cell}$ [J/(kg K)]	900	2500 (+ 300%)	2500 (+ 300%)
$T_{water,\ inlet}$ [°C]	25	26.2 (+ 4.8%)	25.3 (+ 1.2%)

In the initial simulation, the sample cell reached a lower temperature than the physical results. The most effective way to alter this was to change $k_{thermalpad}$. By reducing $k_{thermalpad}$, the thermal resistance over the Peltier elements increased, thus causing heat transfer from the sample to the heat sink to reduce. With the heat transfer reduced, the sample cell would rise in temperature. The constant was optimised to match the respective response of air and vacuum. The change of $k_{thermalpad}$ was also motivated by the thermal contact, which in COMSOL is perfect, but in reality is non-perfect due to dust, air bubbles and other minuscule effects. This difference also exists between air and vacuum, where air molecules help bridge microscopic gaps.

Another issue with the initial simulation was the rapid time response. The heat capacity of the sample cell was therefore increased to change the thermal mass of the system. The choice can also be motivated by the sample cell not being a solid aluminium cylinder. Although the resistor used for the sample cell is a relatively simple construction, there are internal components that change the physical properties of the cell.

Lastly, the setup proved to be highly dependant of the temperature of the cooling liquid. Although the temperature of the real cooling liquid was never confirmed, changing it in the simulation proved highly effective in altering the response of the system. The change in cooling temperature affected most components by changing the achieved steady state temperature. This proved useful when replicating the physical setup.

4

Thermal characterisation of the calorimeter

This chapter will present the results obtained through experimental testing and digital simulation. The results are first validated through signal processing and quality verification to explain the expected accuracy and confidence in the results. The main experimental results are then presented. The main focus of the results is on the sensitivity and calibration coefficient of the calorimeter, but it will also consider how the system operates as a whole. The results will be compared to the digital-twin simulation for an improved understanding of heat flow and physical contributions. Lastly, the error sources of the experiment and simulation will be presented.

4.1 Signal processing

The recorded signal and baseline values are analysed to gain confidence in the accuracy of the measurements. The goal of this section is to explain how the recorded data is handled and used in further calculations. The section will also explain assumptions and choices that have been made during the data analysis process.

4.1.1 Time constant

Deciding how long each laboratory test should last proved to be a compromise between data quality and efficiency. At stage I, a trial-and-error process was used to find that the optimal times for air and vacuum were 6 000 s and 14 400 s, respectively. At this point, the temperature was used to decide the steady state. When the calorimetric setup was altered through various stages, the time constant of the system was expected to change as a result of the change in heat flow. The time constants were therefore verified again, as seen in Figure 4.1. The test was analysed at 5 W to maintain a strong and stable signal. The voltage from the Peltier elements was also preferred, as opposed to the temperature sensors, for better accuracy and stability.

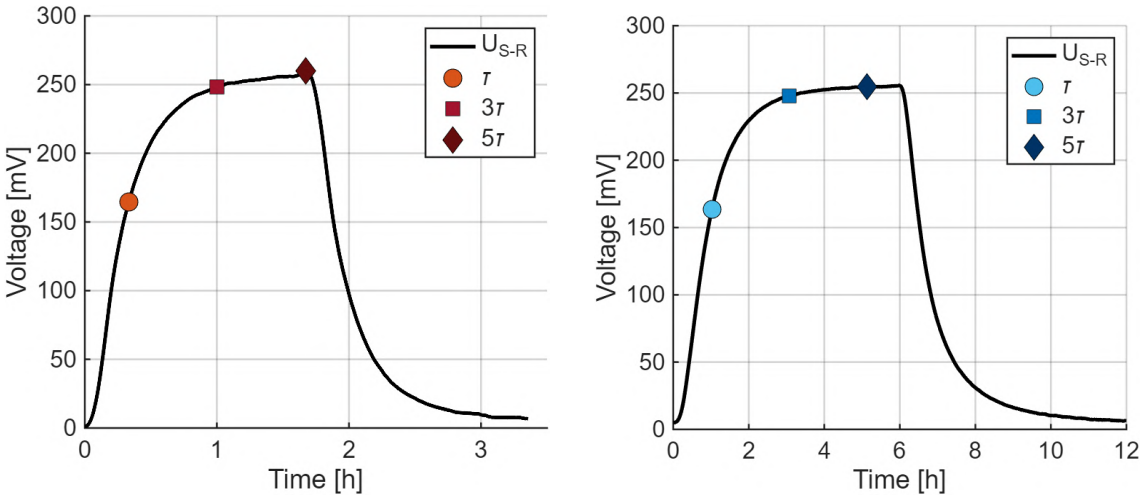

(a) Air **(b)** Vacuum

Figure 4.1: Time constants for air and vacuum at stage IV with 5 W

The figure shows that 5τ is achieved for both air and vacuum. For air, 6 000 s was still used at stage IV and is deemed sufficient since 5τ is reached. For vacuum, the duration of the tests was increased to 6 h, or 21 600 s, to ensure that a sufficient steady state was achieved. As the figure shows, 4 hours was not a bad estimate, as it is above 95% of the total heat development. This can be considered as the bare minimum and can be considered if rapid testing is a priority. With the introduction of overnight-testing in stage IV, 5-6 hours was preferred to achieve a more steady state and increase the quality of the data.

Given the drastic increase in stabilisation time required for vacuum testing, faster methodologies become highly relevant. As established in the theoretical framework, pulse calibration could bypass the need to reach a steady-state plateau entirely. By applying a short thermal pulse and mathematically correcting the dynamic response using the Tian-Calvet equation (2.27), the required testing time could be substantially reduced.

4.1.2 Reference cell and baseline noise

The use of a reference cell can be important for isolating noise from clean measurements. As the reference cell has no applied power, the heat flow over its Peltier elements should, in theory, be zero, indicating no heat exchange between the heat sinks and the reference. However, an experimental setup is never perfect, and the use of a reference sample can help quantify the influence of the surrounding environment. This is more relevant in air, where the ambient temperature can be different from the temperature of the test setup. This effect will be similar for both the reference and the test cell, which means that it can be isolated and excluded by using the measured heat flow from the reference cell.

Another technique for isolating true heat flow is to account for baseline noise in the

Peltier elements. Whether it is an inaccurate voltage across the Peltier elements or failure to reach a thermal equilibrium in the setup, a baseline measurement will reveal such an effect. The baseline offset is recorded after the setup is left to rest, with only the cooling liquid running. The rest period is decided by the time constants for air and vacuum, which were found in the early stages of testing.

Figure 4.2 shows the effect of using a reference cell and accounting for baseline offset. Subfigure 4.2a shows the recorded voltage of the test sample, with no corrections. Subfigure 4.2b includes the reference sample, where it is subtracted from the measured voltage of the test sample. Subfigure 4.2c also subtracts the baseline offset recorded over the test sample. Subfigure 4.2d uses both the reference sample and the baseline offset. Note that the baseline offset for the test and reference samples are not identical and that each measurement is corrected with its respective baseline offset. The purpose of the figure is to investigate the most correct way to handle the recoded values.

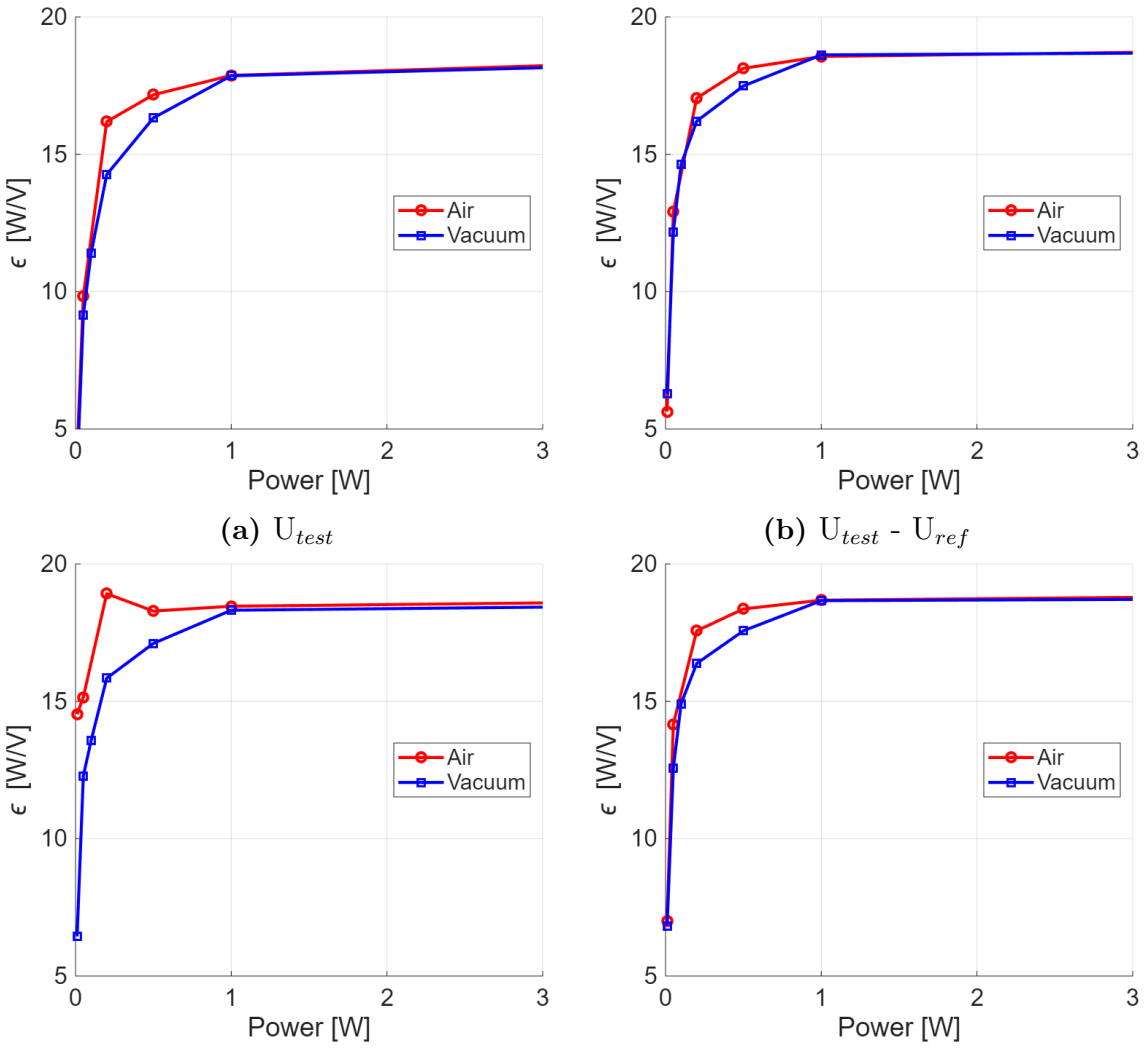

(a) U_{test} **(b)** U_{test} - U_{ref}

(c) U_{test} - $U_{test,offset}$ **(d)** $U_{test,offset}$ - $U_{ref,offset}$

Figure 4.2: Effect of reference sample and offset noise on calibration coefficient from stage I

The figure shows a relatively similar trend for the different versions of ϵ. The overall trend shows that ϵ separates for air and vacuum when the power drops below 1 W. In vacuum, the sample cell gets hotter due to the lack of convection. This forces more heat through the Peltier elements, which increases the voltage output and thus lowers the value of ϵ. The tests were performed in stage I in order to early decide on a preferred method of processing. The correction for both the reference cell and offset baseline is considered the method that best isolates the true heat flow from the sample. The figure also clearly illustrates that the calibration coefficient drops for power levels under 1 W. This is an early indication of the sensitivity of the setup.

With the changes made throughout the process of the experimental testing, the steady state of the setup is expected to change. A change in the baseline voltage is not necessarily good or bad, as the ratio between the peak voltage and the baseline is more important for the calibration coefficient. However, a baseline voltage of 0 mV means that there is no heat flow through the system when resting, since the entire setup is in thermal equilibrium. This also means that each test would show the true thermal response of the system. The recorded baseline voltages for stages I, II and IV at 25°C are shown in Figure 4.3. The voltages are average values found at rest after various power levels.

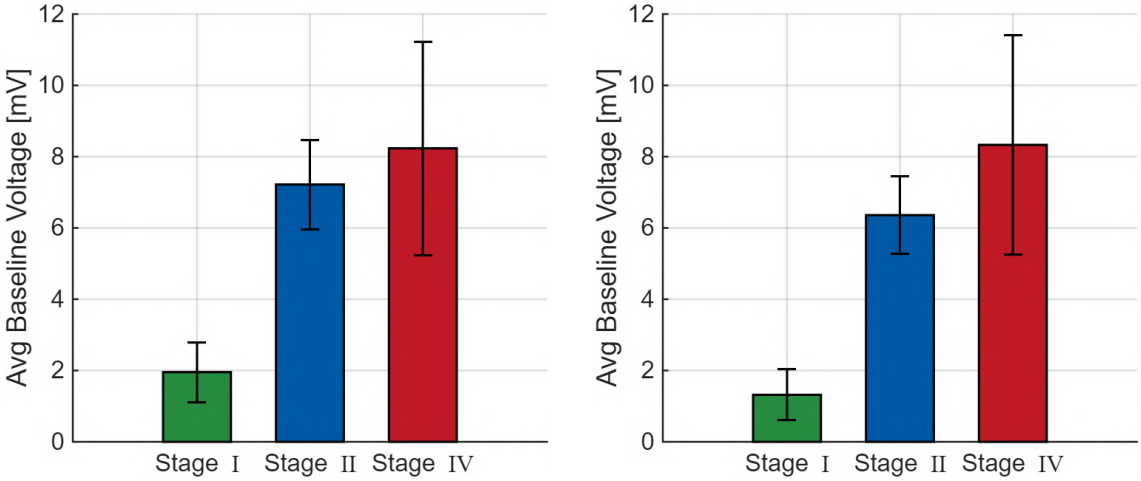

(a) Air **(b)** Vacuum

Figure 4.3: Average baseline voltage for stages I, II and IV at 25°C

The most noticeable difference in the figures is that stage I experiences a significantly lower baseline voltage. In stage I, there were no isolations added to the setup, and the old thermal gap pads were used. The decrease in thermal conductivity from the new Peltier elements means that the temperature gradient increases, and so does the baseline voltage. A similar effect applies for stage IV, where isolation is used. Since isolation works both ways, heat builds up and changes the steady state of the setup, which in this instance means a higher thermal gradient.

It can also be observed that the baseline voltage is slightly lower in vacuum than in air. Although convection is useful for cooling, it also introduces unstable components

to the heat flow. In a vacuum, the setup will rise to a higher temperature, since convection is not present for cooling. However, the heat sink surfaces also increase accordingly, balancing out the thermal gradient across the system and thus lowering the baseline voltage compared to air.

4.1.3 Voltage signals

Throughout the calibration of the calorimeter, the following voltage signals were measured at the different stages of the project, as seen in Table 4.1.

Table 4.1: Voltage signals at different power levels during calibration stage $I - IV$. $Vac_{a,b}$ denotes vacuum and $Air_{a,b}$ denotes air, where a denotes stage testing and b denotes a series testing at each stage.

Stage I				
Power [W]	**Vac**$_{1,1}$ [mV]	**Vac**$_{1,2}$ [mV]	**Vac**$_{1,3}$ [mV]	**Air**$_{1,1}$ [mV]
0.002	-0.84	0.0049	N/A	0.36
0.01	0.32	-0.19	N/A	0.19
0.05	2.73	2.68	2.58	2.24
0.1	N/A	5.63	5.00	N/A
0.5	27.40	21.79	23.56	26.32
1	52.48	46.47	48.44	52.42
5	265.64	264.03	N/A	263.99

Stage II					
Power [W]	**Vac**$_{2,1}$ [mV]	**Vac**$_{2,2}$ [mV]	**Vac**$_{2,3}$ [mV]	**Vac**$_{2,4}$ [mV]	**Air**$_{2,1}$ [mV]
0.5	24.83	23.04	23.10	21.98	26.12
1	50.61	47.79	N/A	43.87	51.64
5	264.65	257.84	263.29	N/A	270.35

Stage III	
Power [W]	**Vac**$_{3,1}$ [mV]
0.5	22.2
1	43.74
5	258.29

Stage IV						
Power [W]	**Vac**$_{4,1}$ [mV]	**Vac**$_{4,2}$ [mV]	**Vac**$_{4,3}$ [mV]	**Air**$_{4,1}$ [mV]	**Air**$_{4,2}$ [mV]	**Air**$_{4,3}$ [mV]
0.5	21.3	23.1	26.24	25.61	25.71	25.42
1	43.94	50.17	50.26	49.04	48.04	51.02
5	252.32	257.44	259.46	245.01	254.13	255.82

Looking at the table, it can be seen that the measurements follow a moderate linear trend for each respective series. The values have a significant variance between different measurements at the same applied power. It is expected that the vacuum will have a higher voltage signal, since more heat will flow through the Peltier

elements. However, no real difference between ambient and vacuum can be observed in the measured voltage signals.

4.1.4 Outgassing

During the initial calibration phase, stage I, variations in the measured values were noted over time. The initial hypothesis was that these changes were caused by material degradation, specifically outgassing of silicone from the used thermal pads exposed to the vacuum environment. To investigate this source of error, follow-up tests were conducted in which the original silicone pads were replaced with corresponding thermal pads based on acrylic.

However, the analysis of these comparative tests showed that the observed measurement variations remained unchanged regardless of the choice of material. This can be seen in Table 4.1 where, for e.g. the signal $\mathrm{Vac}_{2,1}$ at 1 W is bigger than both $\mathrm{Vac}_{2,2}$ and $\mathrm{Vac}_{2,4}$ by a maximum of 6.7 mW. Therefore, the outgassing hypothesis could be rejected. This is also backed up by a visual inspection of the silicone thermal pads, which did not show any signs of outgassing residues. In addition, the maximum operating temperatures of the system were judged to be too low to initiate significant outgassing of silicone, even under low pressure.

4.2 Quality check

To validate the quality of the work done, it can be necessary to check and verify the sensors used. This includes the PT100 sensors and the Peltier elements. After assessing the data from the earlier stages, a theory was introduced suggesting that the vacuum chamber was heated more than expected. In an attempt to understand the reason for the hot chamber, the sensors were calibrated and validated as part of an error source elimination process.

4.2.1 Temperature sensors

In order to verify the quality of the temperature measurements, a sensor check was performed on the PT100 sensors under vacuum conditions. The sensors are left in free space to measure if there is any offset between them. The resulting measurements are shown in Figure 4.4.

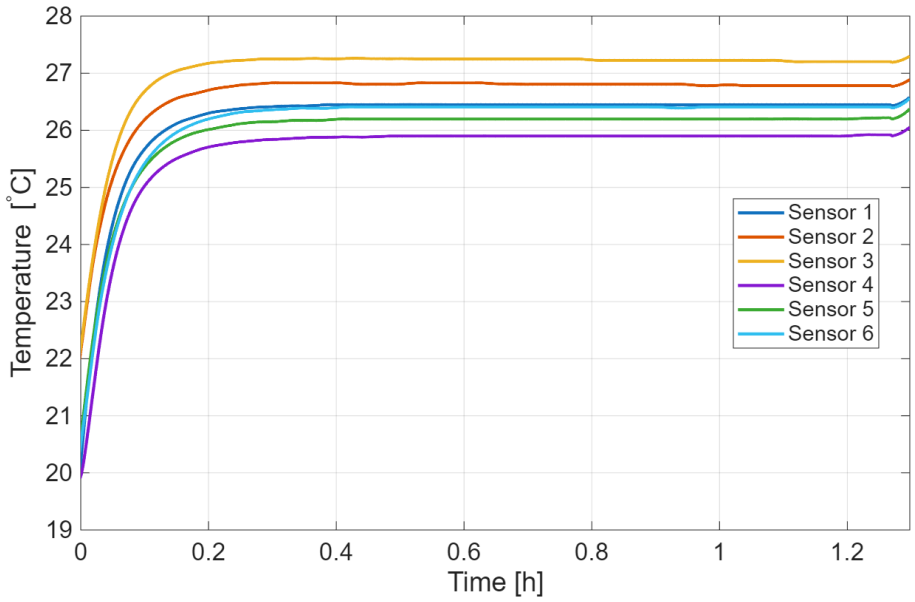

Figure 4.4: Calibration test of PT100 sensors

The figure shows that there is a clear offset between the sensors. As shown in Chapter 3.3.1, the sensors are placed at a similar height and should be affected similarly by radiation and potential convection from the lack of a perfect vacuum. The maximum inaccuracy for the PT100 sensors at 30°C is ±0.151°C. This is lower than the observed difference of 1°C, yet it remains significant to the measurements. There is an argument to be made about the heat transfer from outside the chamber through the cables. However, the cables are brought into the chamber right next to each other, and it's therefore very unlikely to cause a difference of 1°C. The uncertainty of the PT100 cables is not heavily considered in the remaining results, since the trend of the temperature is more important than the specific temperature.

The second calibration test on the PT100 examines how the measurements are affected by the attachment of the sensors to the setup. With the sensors taped on the same heat sink, the system was left to rest in a vacuum with no heat applied. Figure 4.5 shows the resulting temperature recorded by the PT100 sensors.

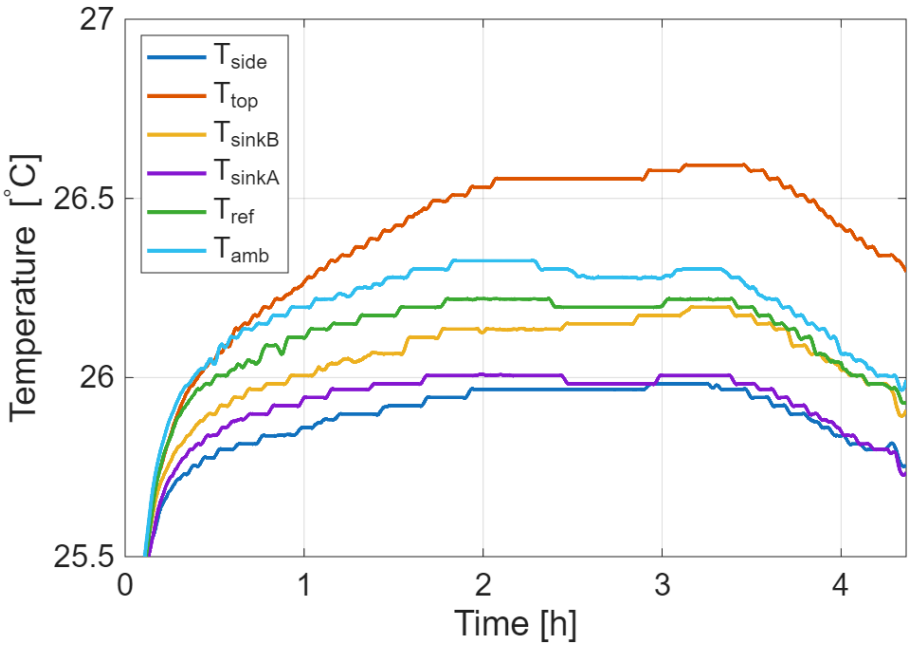

Figure 4.5: Sensor test with PT100 directly placed onto the heat sink and attached with tape

The figure shows that there is still a clear difference between temperature recorded by the sensors. There is a 0.6°C difference at the highest, which extends beyond the PT100 sensor's uncertainty of ±0.144°C at 26°C, yet it is lower than the previous difference of 1°C. The small improvement could come from the sensors being thermally grounded at the heat sinks, thus reducing the apparent difference that exists without contact.

Since it was observed that some sensors remained attached better than others, a more likely theory is that the recordings from the sensors are highly dependent on the thermal connection to the metal heat sink. To verify this theory, a test was performed with different ways of thermally connecting the sensors and the heat sink. The various combinations of electrically isolating tape and thermal gap pad are listed in Chapter 3.3.1. The recorded temperature is shown in Figure 4.6. The test also included applying heat at three different power levels. This was done to understand how the results were affected by an applied heat source.

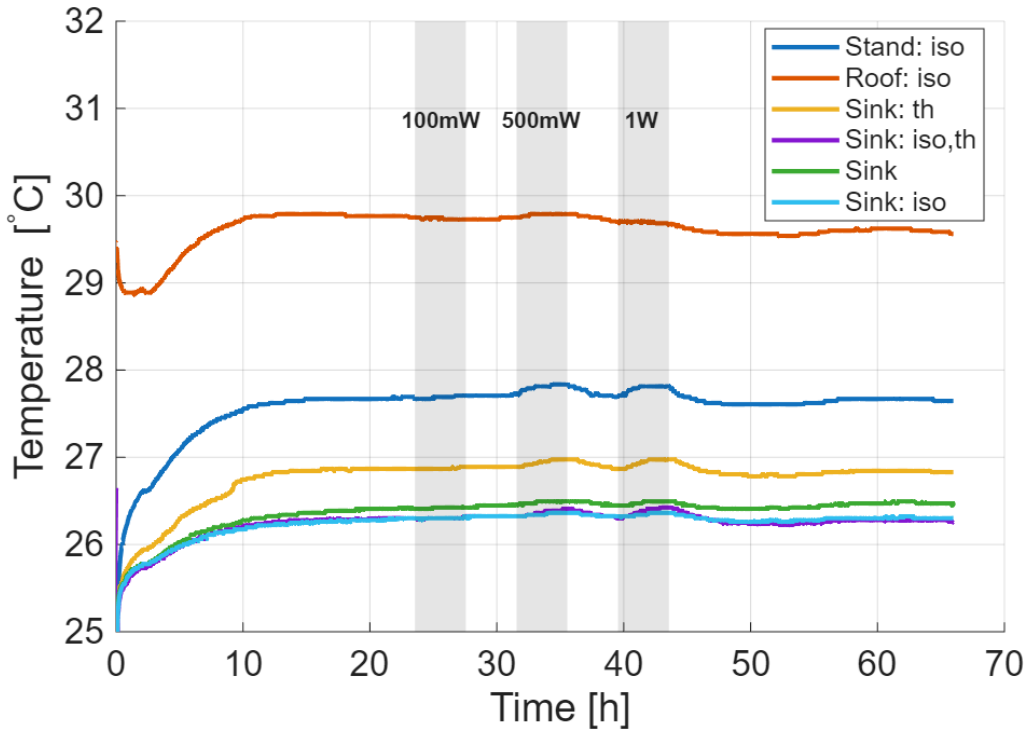

Figure 4.6: Temperature of PT100 sensors with different ways of attachment

From the figure, it becomes clear that the heat sinks remain significantly colder than the stand and vacuum chamber, as expected due to the applied cooling. By inspecting the data from the sensors that were attached to the sink, it's obvious that using an isolating tape is the most beneficial for sufficient contact. It is expected that the better the connection to the heat sink, the lower the temperature. As the heat sink has water circulating at 25 °C, a sufficient thermal contact will bring the recorded values closer to this temperature.

There is virtually no difference between using a thermal gap pad or not, as long as an isolating tape is used. However, without the tape, the data suggests that the thermal gap pad has a worse connection than simply attaching the sensor directly to the sink. Yet again, the quality of the recordings can be questioned. After the experiment, it was observed that both sensors connected using the thermal gap pad had loosened during the experiment. The test proved that the material between the sensor and the heat sink can improve data quality slightly, however, properly attaching the sensors appears to be more important. All experiments have used a Kapton tape to secure the sensors, which have proven not to be reliable in a vacuum.

4.2.2 Peltier elements

The Peltier elements were calibrated by placing a single element alone in the setup. With no convection present, the elements should, in theory, not have a heat flow through them. This means that both sides will keep the same temperature, yielding a voltage of zero. Figure 4.7 shows whether the theory is correct.

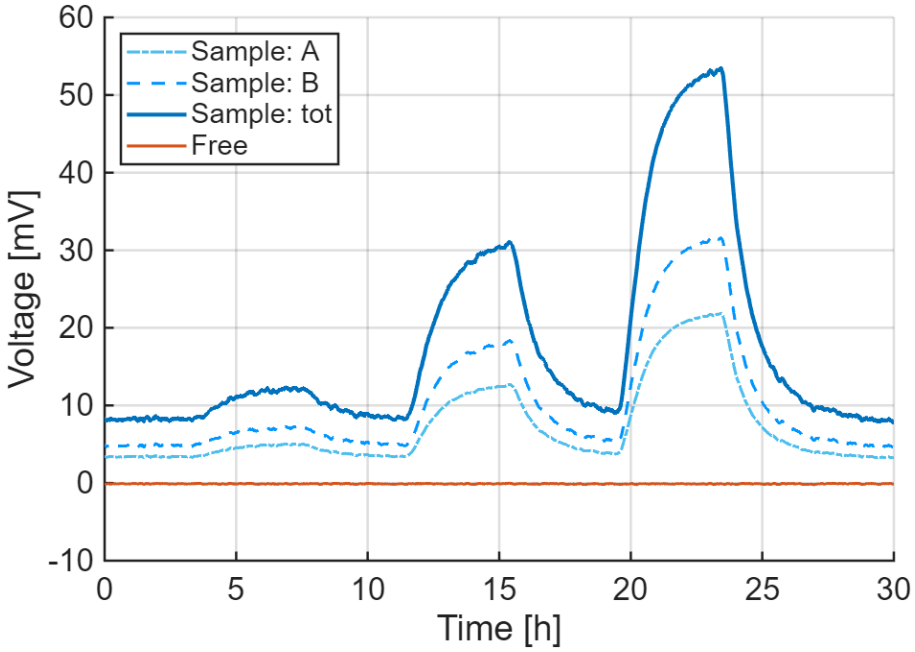

Figure 4.7: Calibration test of Peltier elements on stage II setup using 100 mW, 500 mW and 1 W

The figure shows that the free Peltier element delivers a voltage of only a few microvolts, which in this application can be considered as zero. The figure also compares the recorded voltage to the voltage of the sample when different heat powers are applied. It can be observed that the free Peltier is not affected by the applied heat. This also gives an indication that convection is not present and that the vacuum is sufficient. A clear difference is observed in the signal between A and B sides, suggesting that the heat flow is asymmetrical, potentially from a difference in the cooling capacity of the heat sinks.

To further test the Peltier elements, they were placed in their normal position between the sample/reference and the heat sinks. The calorimeter was opened in order to remove any conductive heat flow through the system. As the new thermal gap pads had higher adhesivity, the elements stuck to different sides and were difficult to remove. Towards heat sink A, the elements stuck to the sample and reference, whilst on heat sink B, they stuck to the heat sink. This test was still deemed useful, as it shows how the recorded voltage is affected by cooling and the surroundings. The resulting measurements are shown in Figure 4.8.

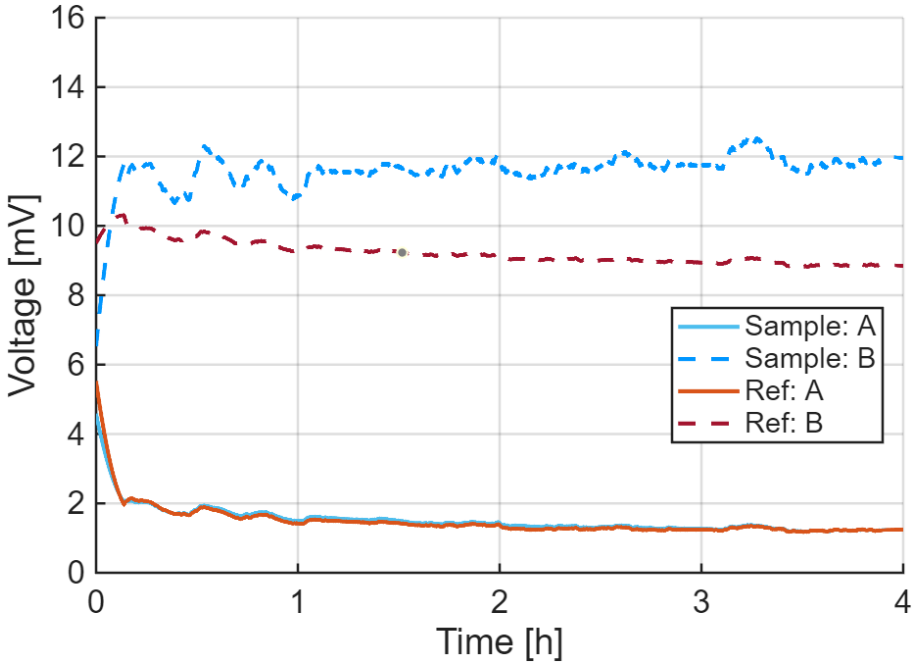

Figure 4.8: Calibration test on Peltier elements with an open stage III calorimeter

The figure shows that the elements stuck on heat sink B return a significantly higher voltage than the elements stuck to the sample and reference. The elements on heat sink B are cooled on one side only. The other side will receive radiation heat from the surrounding chamber at around 30°C. Side A shows a voltage relatively close to 0 mV, proving that the sample, without thermal contact, matches the radiation of the sample holder. Side B shows a noticeable baseline voltage, including a difference between the sample and reference sides. Since side B was slightly closer to the reference than the sample, it could indicate the importance that the view factor has on the radiative heat transfer.

In order to validate the recorded values, it is possible to calculate the theoretical expected voltage based on the surface temperature and the Peltier elements' Seebeck coefficient. The results of this are shown in Table 4.2. The calculation includes a view factor which aims to simulate the open setup being slightly skewed. The inclusion of the view factor is also to visualise deviations in the voltage.

Table 4.2: Theoretical voltage of peltier test

Peltier element	$\mathbf{T}_{surface}$ [°C]	**View factor**	$\mathbf{Q}_{rad}$ [mW]	$\mathbf{U}_{expected}$ [mV]
Sink A - Sample	26	0.9	30	1.97
Sink A - Ref	26	1	33	2.19
Sink B - Sample	18	1	160	10.54
Sink B - Ref	18	0.9	144	9.49

By comparing the theoretical and measured values, a strong correlation is observed. The Peltier elements will be heated by radiation on the side that is left open to the vacuum. For sink A, the theoretical values are found to be around 2 mV, whilst the recorded values dip closer to 1.2 mV. This difference of 0.8 mV is considered extremely low compared to the system noise. For heat sink B, the measured values around 12 mV and 9 mV also correspond well to the expected theoretical values of 10.54 mV and 9.49 mV for the sample and reference, respectively.

It is worth mentioning that the calculations are not perfect, as they do not simulate the true view factor from the setup around it. Similarly, it does not include other heat sources such as reflection from neighbouring components.

4.2.3 Isolation

The focus was then shifted to why the chamber walls were so hot in a vacuum environment with negligible convection. This prompted the test to see how the surrounding laboratory temperature affects the inside of the chamber. Figure 4.9 shows the resulting comparison of three sensors and the ambient lab temperature. The three sensors are placed on heat sink A. The temperature sensor in the lab is placed about 2 meters from the vacuum chamber, at the same height, obtaining a realistic comparison for the chamber.

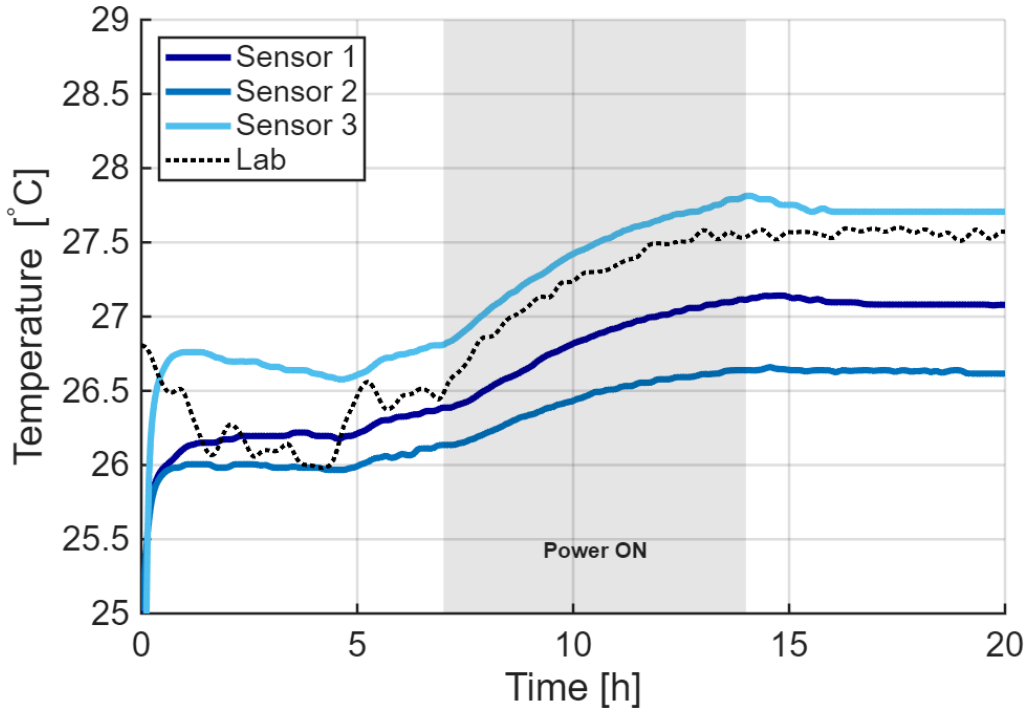

Figure 4.9: Temperature of laboratory (outside chamber) compared to inside the chamber during a 7-hour test at 1 W

The figure shows a clear correlation between the lab and chamber temperature. Since a 1 W test is highly unlikely to affect the ambient temperature of the laboratory, it

can be assumed that the temperature increase seen on heat sink A is driven by the ambient lab temperature.

To further quantify the effect of the surrounding lab temperature, a correlation coefficient can be seen in Table 4.3. Sensor 3 and the average of the three sensors are used to validate the coefficient. Figure 4.9 is shown as test 3 in the table. The correlation coefficient was compared over four different tests, where the various heat power and duration are found in Table 4.3.

Table 4.3: Correlation coefficient between lab and heat sink temperature

Correlation	**Sensor average**	**Applied heat power**
Test 1	0.845	0 W @ 4h
Test 2	0.919	0.1, 0.5 & 1 W @ 4h
Test 3	0.878	1 W @ 7h
Test 4	0.823	1 W @ 12h
Avg	0.866	

The correlation varies between perfect (1) and non-existent (0), where the table shows that the correlation between the lab and chamber temperature is relatively high. This implies that the chamber is significantly impacted by the surrounding temperature. This will result in higher radiation onto the setup in vacuum and a higher convective heat effect in air. This additionally proves a shift of the baseline during calibration.

As mentioned in Chapter 3.3.3, the change from stage II to IV included adding isolation inside and around the vacuum chamber. The results from this test are shown in Figure 4.10. This figure will visualise the impact of the isolation used. The figure shows the temperature of heat sink A and the base of the stand, in addition to the voltage produced over the Peltier elements.

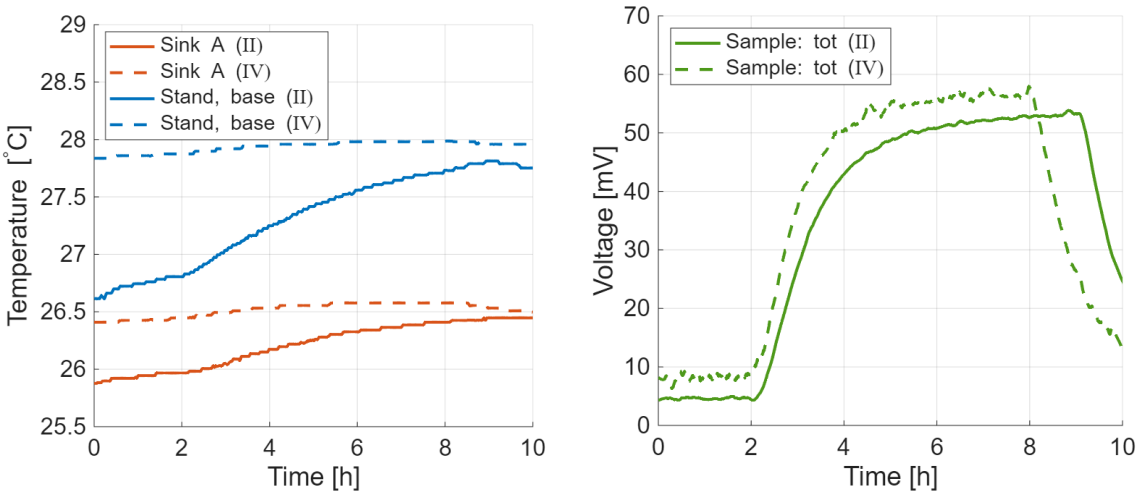

(a) Temperature **(b)** Voltage

Figure 4.10: Isolation test at 1 W comparing stage II and IV with added isolation

Figure 4.10a shows that there is a visible difference in temperature, especially on the stand base. With the added isolation, the temperature appears to increase, which goes against the initial idea of the test. This suggests that the heat flow from the sample/setup to the chamber flows in the opposite direction of what was initially thought, and is now reduced or blocked. Furthermore, it shows that the stand and heat sink are now less affected by the applied heat power and remain significantly steadier.

When observing the voltage profile, it is clear that the isolation increases the voltage by a constant value of around 5 mV. This is supported by the observed temperature, suggesting that the isolated system has its steady state at a higher temperature and is therefore less affected by the 1 W of applied power. On one side, the increased steady state temperature of the isolation can be useful to ensure stable testing. On the other side, the voltage is now further from the idealised baseline voltage of 0 mV. However, a 0 mV baseline primarily promotes stable recordings and does not necessarily affect the calibration coefficient of the setup.

4.2.4 Measurement accuracy

For stage I, a significant amount of data was collected. Although stage I was a trial-and-error phase, the data are still deemed useful to understand the accuracy of the measurements. By comparing several tests at each power level, an error estimation can be found. Figure 4.11 shows the change in the calibration coefficient for stage I tests. Each power level value is the average of three or more datasets. The spread in data is shown by the shaded areas.

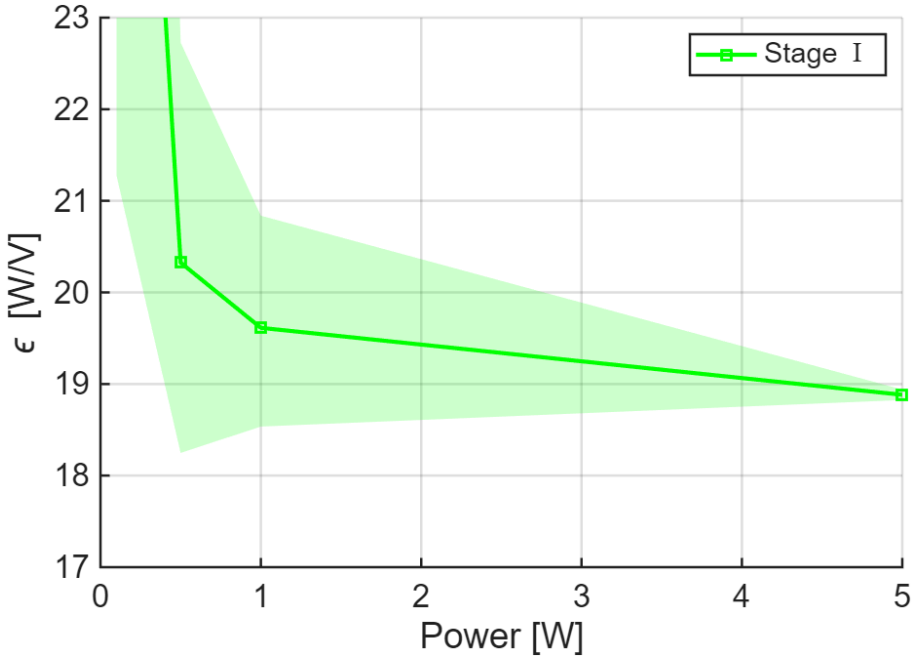

Figure 4.11: Calibration coefficient for stage I vacuum, comparing with and without a reference sample

It is observed that the value of ϵ and its accuracy change significantly at lower power levels. With lower heat power, the signal drowns in the noise and ambient heat that is present. This trend is also supported by the highly accurate 5 W measurements, where the applied heat dominates.

4.3 System performance

This chapter is dedicated to the analysis of the performance of the complete system. Although it is important to investigate the temperature and heat flow inside the chamber, the most crucial value is the calibration coefficient.

4.3.1 Sensitivity

The Peltier elements are the foundation for measuring the heat flow from the sample cell. Since they generate a voltage from a temperature difference, it is valuable to investigate the sensitivity of the elements. This will reveal how low a heat flow is possible to record with confidence. Figure 4.12 shows a stage IV vacuum test run at 50 mW, 100 mW and 500 mW, with the intent to reveal a sensitivity limit.

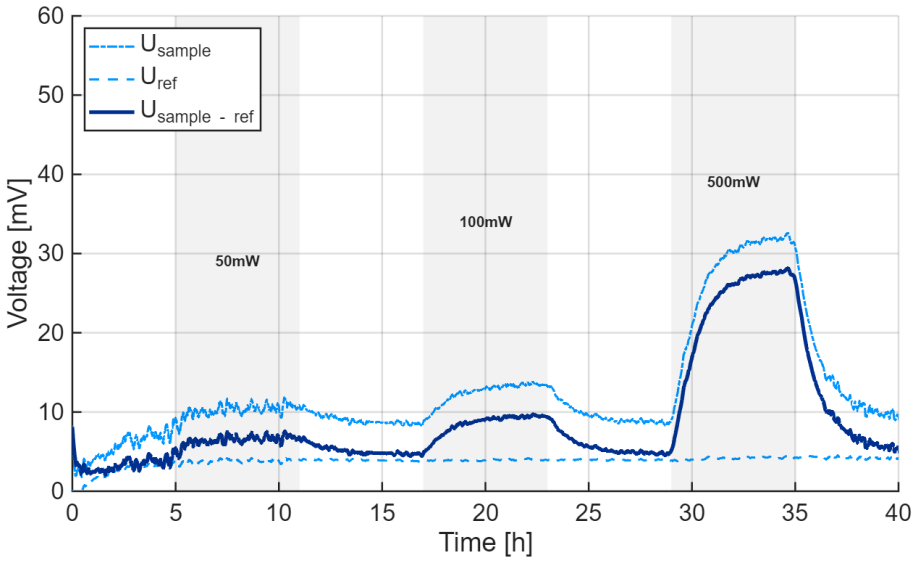

Figure 4.12: Recorded voltage of stage IV vacuum at 25 °C

The figure shows a clear distinction in the quality of the measured signal. At 100 mW and 500 mW, the system is clear and shows an obvious trend. At 50 mW, the signal experiences significant fluctuations and fails to stabilise. There is a visible rise in the voltage at 50 mW, but it is only a few millivolts, which in this context is considered unstable compared to the observed fluctuations. The figure suggests that a sensitivity limit exists between 50 mW and 100 mW, since the system then struggles to differentiate between applied power and ambient noise. This is a potential limit found strictly based on the voltage signals. External factors can affect the sensitivity of the full setup. It is worth mentioning that if a 0 mV baseline were to be achieved with a system in thermal equilibrium, the system sensitivity could potentially be lower.

4.3.2 Calibration coefficient

The calibration coefficient is arguably the most important value of the calorimeter setup, as it can translate the recorded voltage into an estimated heat flow. This is a key fixture when analysing the heat development in a cell. The calibration coefficient has experienced changes in values and trends through the various stages of the lab setup. Figure 4.13 illustrates the calibration coefficient across stages I and IV. Note that stage I has been averaged over several tests at each power level to compensate for unstable measurements.

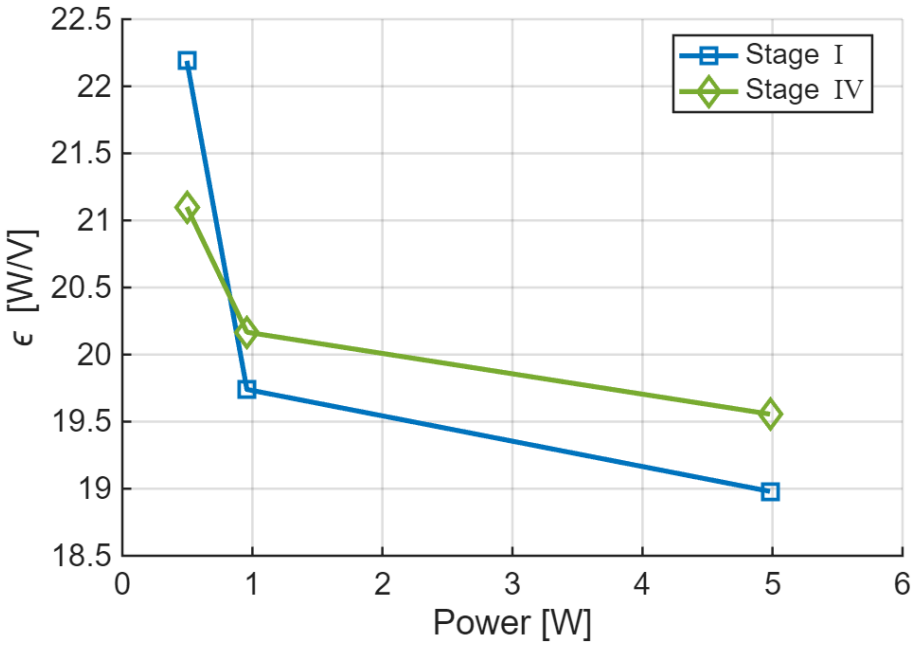

Figure 4.13: Calibration coefficient for stages I and IV

Throughout the report, an ϵ value closer to the theoretical value of 15 W/V has been considered good. As calculated in Appendix A.1, the theoretical value is based on the material properties of the Peltier elements and is not representative on a system level, where heat losses occur. With heat losses, the value of ϵ is expected to increase. By the same logic, the figure suggests that stage I is better and more accurate compared to stage IV. The calibration of the calorimeter does not depend on the exact value of ϵ, but on its stability. Since the calibration coefficient ideally should be identical for all power levels, the change in ϵ is more important in Figure 4.13. Stage IV shows the steadiest behaviour, indicating that the changes made to the setup have improved the stability.

With the final stage IV configuration, the system is at its most optimised state. This means that the recorded values provide the most accurate representation of the heat development. Figure 4.14 shows the calibration coefficient for air and vacuum at stage IV. To validate trends, the figure compares two differently corrected values. The offset values subtract the recorded baseline, whilst the net value also corrects for the reference and its respective offset. The net values are considered the most accurate because they remove both signal noise and surrounding heat flow.

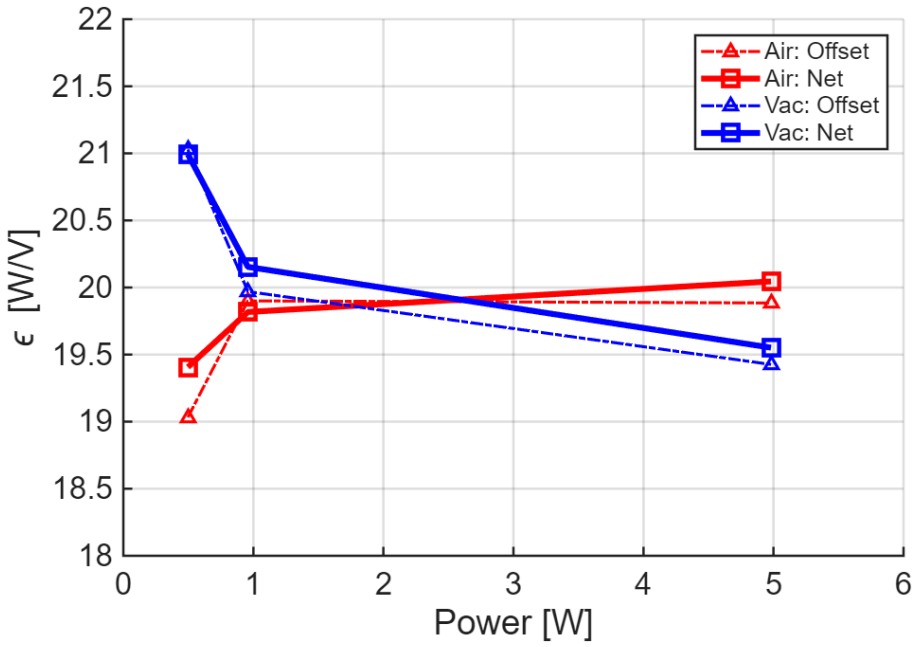

Figure 4.14: Calibration coefficient for air and vacuum in 25°C at stage IV

The figure shows a relatively steady trend at 1 W and 5 W for both air and vacuum. The average values at these levels are found to be 19.93 and 19.85 W/V for air and vacuum, respectively. Although ϵ is slightly lower for vacuum, their similarity proves that the vacuum setup must be improved to achieve a considerably lower ϵ. When the applied heat power drops below 1 W, the recorded heat flow is disrupted by the surroundings. With the 500 mW test included, the average calibration coefficient is now 19.76 and 20.23 W/V for air and vacuum, displaying the stability of the air in contrast to the uncertain behaviour of the vacuum test. This additionally proves that the sensitivity of the stage IV setup is closer to 1 W, which is significantly higher than the previously assumed sensitivity of 50-100 mW. Although it is possible to record a heat flow at power levels down to 50 mW, the system is too disturbed by the surrounding environment to provide valid results.

When the power drops under 1 W, there is a clear separation between air and vacuum, where they continue in opposite directions. A reduction in ϵ means a higher heat flow through the Peltier elements. The figure thus suggests that the heat flow is overestimated in air, likely from the balancing effects of the convection. In vacuum, the heat flow is underestimated, showing that losses are increasingly dominant at low power levels.

4.3.3 Thermal sensitivity on the calibration coefficient

When stages III and IV were initiated, a decision was made to lower the cooling temperature to 15°C. This was done to investigate how a colder system would respond to the ambient chamber temperature. After several tests at a lower cooling temperature yielded similar results, a test at a higher cooling temperature was also

included to enforce the potential pattern. Figure 4.15 shows how the calibration coefficient of the system changes based on the applied cooling temperature.

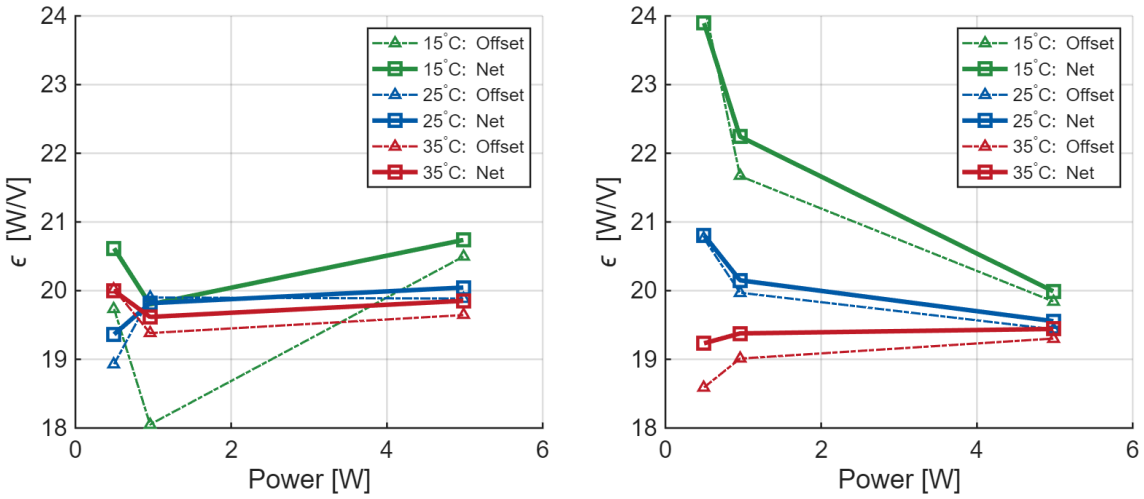

(a) Air **(b)** Vacuum

Figure 4.15: Calibration coefficient for 15°C, 25°C and 35°C for stage IV

The figure shows a clear trend where ϵ appears to decrease as the temperature increases. Although the trend is clear, the order of magnitude is not linear between the tests, meaning a 10°C increase or decrease did not yield the same deviation from the original 25°C. This is likely due to the equilibrium state of the system. With the chamber walls being 28-30°C, the system is more stable at a higher cooling temperature. With the cooling set to 15°C, there is an increase in the radiation to the heat sink.

A working theory is that there exists a perfect temperature to run the current stage IV setup. That ideal temperature is likely the same as the chamber walls. With the entire setup at the same temperature, there will be no radiation as there are no temperature gradients. In theory, the Peltier elements would then record a baseline voltage of 0 mV. When the heat is applied, the recorded response would be from the heat source alone, with no external effects. This should give the true voltage and potentially a calibration coefficient closer to the theoretical value of 15 W/V.

Another observation from Figure 4.15 is the direction that ϵ has between 500 mW and 1 W between the different temperatures. In air, the difference is relatively insignificant, proving the stability that convection provides. In vacuum, the losses present at lower power are significantly more impactful than in air. The trend in vacuum appears to be consistent, with a larger temperature difference producing a more deviating ϵ. The reversed heat flow at 35°C that causes the opposite behaviour in ϵ, illustrates the possible existence of a perfectly stable ϵ that is not reliant on the applied power.

With the cooling system set to 35°C and the chamber temperature normally being recorded at 28-30°C, the heat flow of the system is reversed. The hotter heat sinks

will radiate onto the setup and the surrounding walls. The resulting heat flow will generate a negative voltage over the Peltier elements, as shown in Figure 4.16.

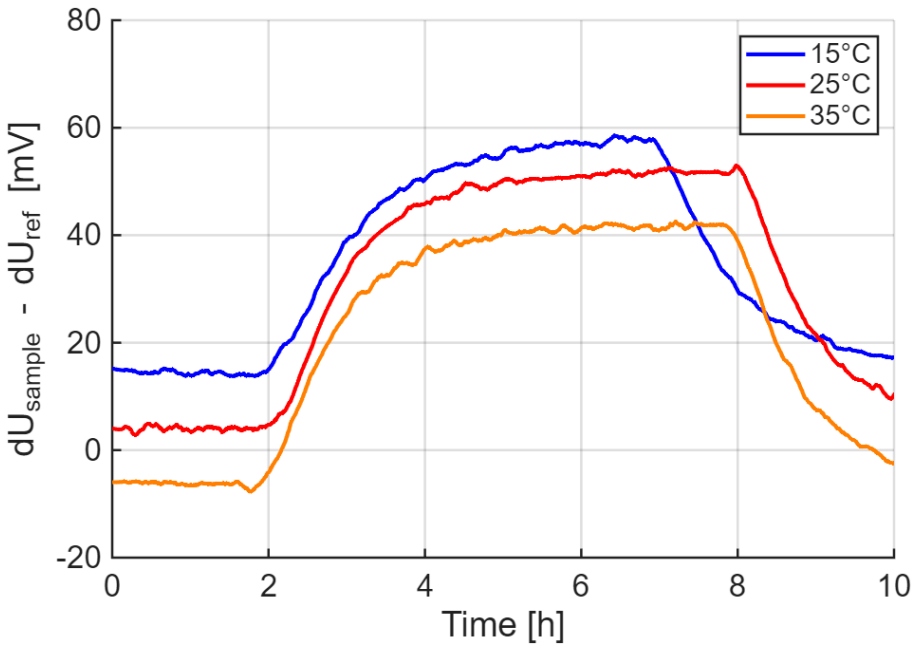

Figure 4.16: Voltage response at 1 W for 15°C, 25°C and 35°C at stage IV vacuum

The figure shows a clear distinction in the recorded voltage from the Peltier elements, where the temperature of the coolant is an important factor. At 35°C, the baseline voltage is observed to be negative, confirming the reversed heat flow through the system. The baseline voltage increases as the cooling temperature decreases, indicating a change in temperature gradient over the Peltier elements. This relation is directly linked to the behaviour of the calibration coefficient.

When comparing 15°C and 25°C, it is observed that the gap between the baseline voltages is higher than the gap at steady state heating. This shows how ϵ will increase for 15°C. Similarly, the negative baseline at 35°C will increase the total voltage difference and thus decrease ϵ, as shown previously. The baseline voltages is shown in greater detail in Figure 4.17, where *net* refers to the sample voltage minus the reference voltage, with both being corrected for baseline voltage.

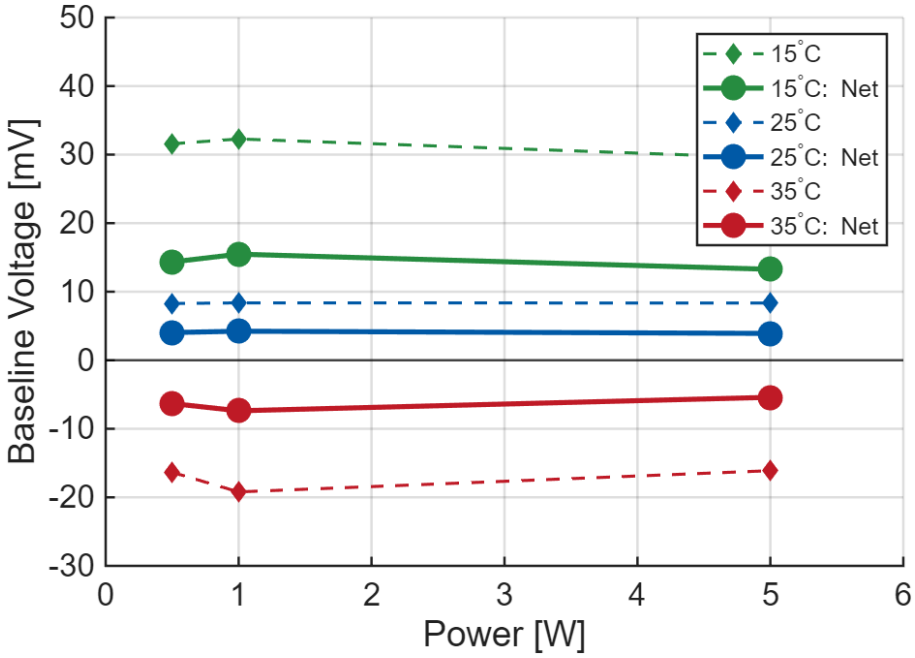

Figure 4.17: Baseline voltage of stage IV at 15°C, 25°C and 35°C in vacuum

The figure shows how the baseline voltage drops to a negative value as the heat flow is reversed. This supports the working theory of a possible baseline voltage of 0 mV. It can be observed that the baseline voltages remain relatively stable for the different power levels. This indicates that the time constant is sufficient to reach a stable resting state.

4.3.4 Temperature

For the improvement of the intended calibration method, the temperature of the sample was analysed during the experiments. Most looked at was the temperature of the aluminium block surrounding the dummy cell. Comparisons of its maximum temperature reach in air and in vacuum at different cooling temperatures are shown in Table 4.3.

Table 4.4: Max temperatures at different power levels and cooling temperatures

25°C						
Power [W]	**Vac**$_{Stage\ I}$ [°C]	**Vac**$_{Stage\ II}$ [°C]	**Vac**$_{Stage\ IV}$ [°C]	**Air**$_{Stage\ I}$ [°C]	**Air**$_{Stage\ II}$ [°C]	**Air**$_{Stage\ IV}$ [°C]
0.5	25.5	26.2	26.67	25.6	25.5	25.8
1	25.8	26.5	27.2	25.8	25.8	26.0
5	27.8	28.7	31.0	27.5	27.8	28.3

15°C		
Power [W]	**Vac**$_{Stage\ IV}$ [°C]	**Air**$_{Stage\ IV}$ [°C]
0.5	19.4	17.9
1	20.0	18.0
5	23.7	19.9

35°C		
Power [W]	**Vac**$_{Stage\ IV}$ [°C]	**Air**$_{Stage\ IV}$ [°C]
0.5	33.9	34.2
1	34.2	34.5
5	37.9	36.6

From the Table 4.3, some noticeable comparisons can be made between air and vacuum. It can be observed that the system during higher power levels (5 W) shows a clear increase in thermal resistance, leading to a much bigger max temperature in vacuum than in air at 15°C and 25°C. This can be seen as a result of the exclusion of convection in a vacuum, resulting in exclusive reliance on thermal conduction and radiation.

Consequently, at cooling temperatures at 35°C and lower power levels (0.5 - 1 W), the opposite can be observed as the max temperature is hotter in air than in vacuum. This implies that the air in this case acts as a convective heat source. Though at 5 W, the heat generation from the sample cell exceeds the temperature of the surrounding air.

Between the different stages I-IV at 25°C, a noticeable difference in the maximum at the same power levels was observed. This increase in maximum temperature indicates a significant increase in thermal accumulation for the system in vacuum over time. The increase can be a result of the many different factors that changed during the stages, including the change of thermal pads, usage of isolation, and also removing and reattaching the Peltier elements.

Lastly, it was observed that between the different cooling temperatures at 5 W, the temperature difference decreases between air and vacuum as the temperature of the water increases. Going from ΔT of 3.8°C at 15°C to a ΔT of only 1.3°C at 35°C. This observation confirms the radiation's non-linear behaviour, as at higher temperatures the radiation from the aluminium block becomes bigger, compensating for the loss of convection in the vacuum.

4.3.5 Cooling

The Julabo cooling system is rated for 220 W and 15 L/min, however a confirmation test was deemed necessary to verify the flow rate. By measuring the flow rate out of the pump into a measuring cup, a water flow of roughly 6.5 L/min was established. From the recorded water flow, it is possible to estimate the speed of the water within the heat sink loops. This will also make it possible to estimate a Reynolds number, which will tell if the cooling system operates with laminar or turbulent flow. The estimated values are shown in Table 4.5. Since it was observed that the T-connection used to split the water flow is not placed fully horizontal, it is assumed a 40-60 split, where heat sink B receives 60% of the water.

Table 4.5: Estimated water flow through the heat sinks based on measured flow rate

Variables	**Sink A**	**Sink B**
$\dot{V}_{pump}$ [L/min]	6.5	
Flow split [%]	40	60
$\dot{V}_{split}$ [L/min]	2.6	3.9
$V_{inner\ loop}$ [m/s]	1.36	2.04
$Re_{inner\ loop}$	7 480	11 220
ΔT at 5 W [°C]	0.028	0.018

Since turbulent flow is assumed to be fully present at $Re > 4\ 000$, it is safe to assume that the cooling system is operated with turbulent flow. This provides much more efficient cooling than laminar flow, due to the internal mixing and heat transfer of the water. The temperature difference within the cooling circuit is also estimated to increase by a maximum of 0.03°C at the highest applied heat power of 5 W. This is considered negligible compared to the temperature increases elsewhere in the setup.

The temperature of the cooling liquid is assumed to be constant. However, the temperature at the heat sink surfaces has been observed to differ. Figure 4.18 shows the temperature of heat sink A in air and vacuum. The figures have been overlapped with the voltage of the Peltier elements to indicate when the heat power is applied.

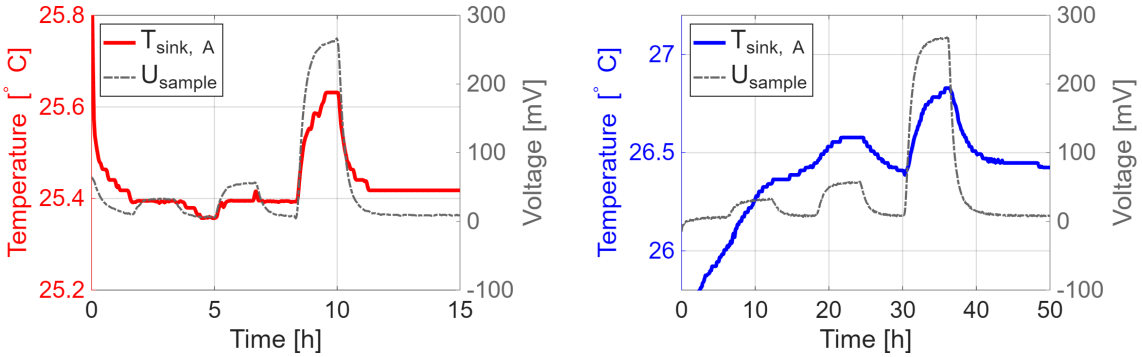

(a) Air **(b)** Vacuum

Figure 4.18: Temperature of heat sink A with applied heat of 500 mW, 1 W and 5 W at 25°C cooling

At 500 mW there is a negligible contribution to the recorded temperature of the heat sink surface, both for air and vacuum. At 1 W, the contributions start to become visible in vacuum, whilst they are only slightly present in air. This difference comes from the convection of the air, which keeps the heat sinks and setup cooler. At 5 W, there is a clear response in the temperature for both air and vacuum. The response in air is now significantly more visible as the heat power overcomes the cooling effects of the convection. Despite this, the temperature response is greater in vacuum, with an increase of around 0.5°C, compared to 0.2°C in air. The figure makes it clear that the heat sink surfaces are affected by the applied thermal power. This gives an indication that the cooling setup might not be sufficient. Comparing this to the estimated water flow found previously, it could indicate that the heat sink setup should be redesigned, as there is a significant temperature gradient within the sinks.

The cooling capability of the system at different temperatures is analysed by comparing the recorded heat sink temperature. The results are shown in Figure 4.19. The data is normalised to its respective cooling temperature

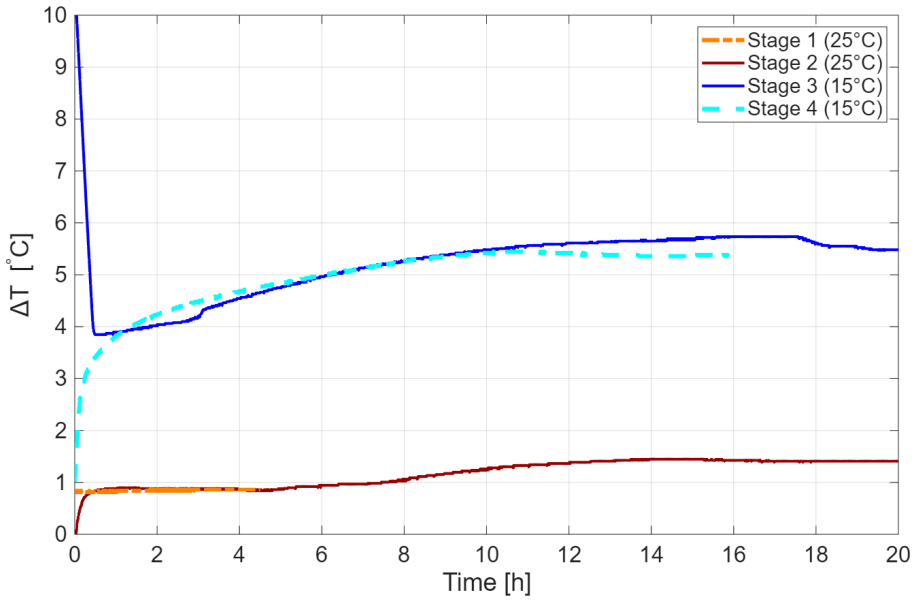

Figure 4.19: Temperature on heat sink A at different cooling temperatures in vacuum

The figure shows a clear distinction between the 15°C and the 25°C cooling, where 15°C cooling experiences a significantly higher increase from its set value. For 25°C, the increase only amounts to about 1-1.5°C, whereas at 15°C, the increase is a staggering 5-6°C from the temperature it's supposed to be. This reinforces the suggestion that the cooling system is lacking capacity and could benefit from a redesign. With sufficient cooling, the heat sinks should be able to remain at the set cooling temperature despite their surroundings.

However, with a heat sink at a lower temperature, the radiation effects from the surrounding chamber are increased as it follows T^4. Since the temperature sensor is placed on the top surface of the heat sink, an increase in radiation could heat up both the top surface and the sensor itself. A temperature sensor inside the cooling system would be necessary to confirm the actual cooling temperature in the heat sinks. This would confirm if the pump circuit is sufficient or if the heat sinks themselves need to be changed.

It is shown in the calorimeter setup that a T-connection is used for the water. With enough pressure, the cooling water should disperse equally to both sides. However, the T-connection is slightly tilted, which means that if the water pressure is not sufficient, gravity will feed more water into one side. Figure 4.20 compares the temperature of heat sink A and B for tests at 15°C, 25°C and 35°C. The figure will help confirm if the 40/60 split assumption in Table 4.5 is correct.

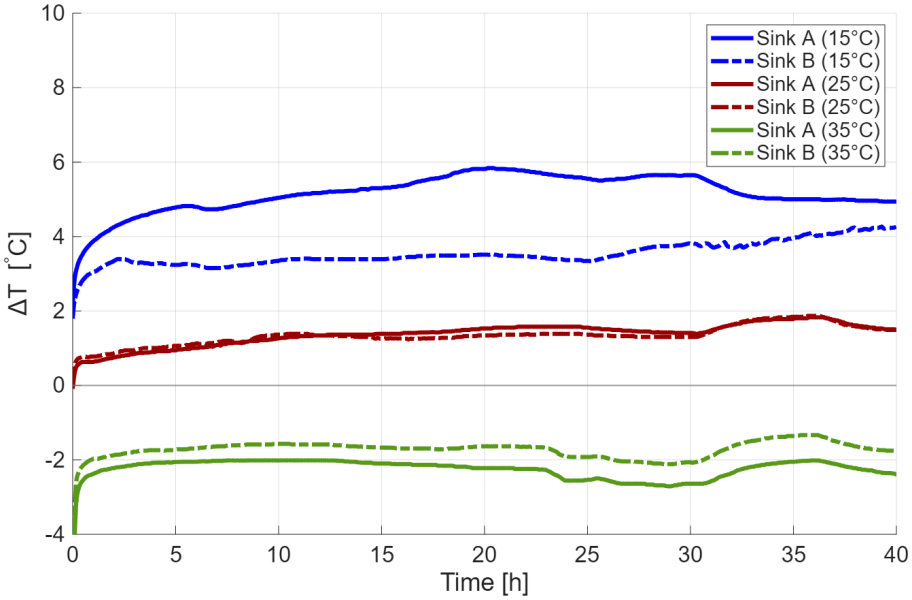

Figure 4.20: Temperature of heat sink A and B at stage IV in vacuum

The figure supports the theory of insufficient pressure and unequal cooling capacity, where a clear distinction is seen between heat sinks A and B at 15°C. The difference is larger at lower cooling temperatures due to the altered heat balance of the system, where the cooling fights against a larger temperature difference compared to the surroundings. This is also seen at 35°C, where the temperature difference to the surroundings is lower, but negative as the heat sinks heat up the surroundings. Notice that sink B still maintains the lowest absolute temperature, proving its increased capacity over sink A. Although the 40/60 split assumption is less present at 25°C due to its low temperature difference to the surroundings, it is further confirmed by the Peltier elements in Figure 4.7.

In air, the heat sinks are aided by convection to remain cool. In a vacuum, the heat from the sample is transferred through the Peltier elements and into the heat sink via conduction. Since the heat has no air around it, it remains in the heat sink, thus heating it up. The thermal resistance of the aluminium heat sinks can cause the heat to spread unevenly. The heat gets stuck at the edges, whilst the core of the heat sinks is cooled. Since the temperature sensors are placed on the top surface, they are likely to experience a higher temperature in vacuum compared to air. Table 4.6 compares the temperatures of the heat sinks in air and vacuum for stage IV. The values are an average over a test with 500 mW, 1 W and 5 W applied throughout.

Table 4.6: Difference in temperature between the heat sink surface and the cooling

$\mathbf{T}_{cool}$ [°C]	**Avg ΔT (air)** [°C]	**Avg ΔT (vac)** [°C]
15	1.83	3.96
25	0.48	0.70
35	-0.64	-1.91

The table shows a clear distinction between the air and vacuum tests. This shows the effect that convection has on the heat sinks. With air present, the heat sinks are able to remain relatively cool compared to the vacuum test. The table also highlights the increasing difference in temperature as the cooling temperature is changed. In vacuum there is a significant increase between 15°C and 25°C cooling, of 0.70°C and 3.96°C, respectively. This observation indicates that the heat sinks are unable to maintain a stable cold side reference for the Peltier elements. When the cooling temperature is increased beyond the surrounding lab temperature of 28-30°C, the heat flow is reversed, and the heat sinks experience a negative gradient.

4.3.6 Theoretical heat generation in battery cell

The observed results can be compared to the battery cell for which the setup is designed by simplifying the heat generation. Since the full thermal profile of the battery cell would require a more in-depth investigation, the reversible heat is neglected, meaning only the irreversible heat is considered. The cell has an internal resistance of 3 mΩ and a capacity of 33 Ah. The resulting heat generation is presented in Table 4.7. The relevant load on the cell is assumed to be in the range of 0.1C to 0.5C.

Table 4.7: Simplified heat generation from the large-format cylindrical battery cell

C-rate	**Current** [A]	**Heat** [mW]
0.1	3.3	33
0.2	6.6	131
0.3	9.9	294
0.4	13.2	523
0.5	16.5	817

At the assumed C-rates, the cell is estimated to produce around 30-800 mW of heat. Since this is a simplified case, the true heat profile can be both higher and lower,

depending on the entropic behaviour of the cell. An important consideration from this estimation is the range for which the calorimeter should be used. With the Peltier elements being able to record values confidently at 100 mW, the sensitivity is close to being sufficient. However, since the heat generation does not surpass 1 W, the calibration coefficient is expected to be unstable and non-linear. These results prove that the current setup could be useful at C-rates over 0.5, but will need improvements to confidently measure the desired range of C-rates.

4.4 Physics-based solutions

To better understand the measured results, a physics-based digital twin was modelled to try to replicate the observed results. The model solutions are limited to 1 W of power from the sample. The results analysed are to be seen as support for the analyses that have been made and hypotheses formed based on the experiments that have been performed.

4.4.1 Temperature profiles

In order to validate the model, the temperature profiles of the simulated modules were compared to the measured experiments. The temperature was chosen as a validating parameter, as it was experienced to be as important as the heat flux (calibration coefficient) for the experimental measurements. Figure 4.21 shows the comparison between COMSOL simulations and the recorded temperature for the different stages. All recordings have been normalised to start at a cooling temperature of 25°C. This has been done to highlight the actual change in temperature and reduce the impact of residual heat.

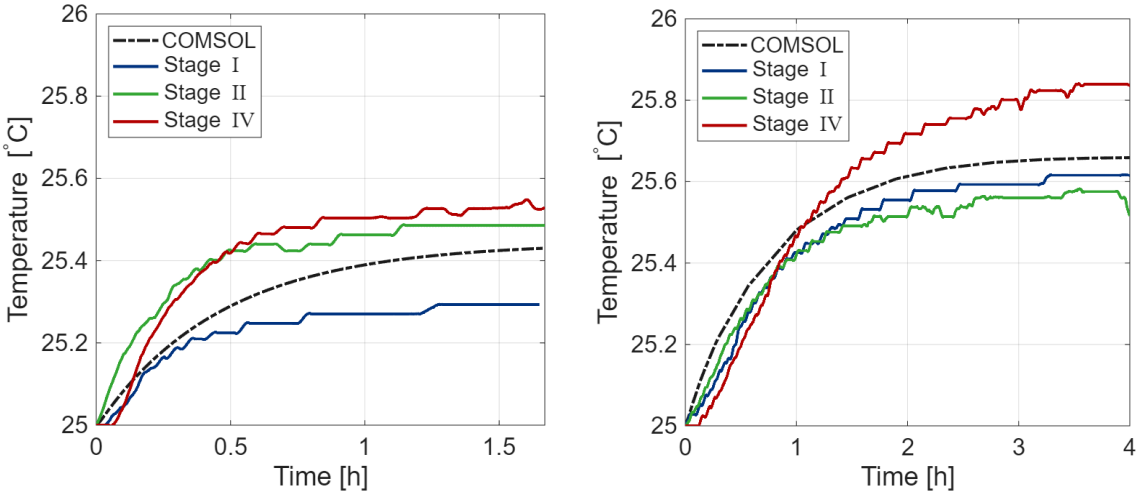

(a) Air **(b)** Vacuum

Figure 4.21: Side of core temperature for COMSOL and stages I,II and IV

The figure shows a clear correlation between the simulated and recorded temperatures. Since the simulated values are based on a surface integral corresponding to

the location of the sensor placement, the values are not expected to be a perfect match. Contact resistance will play a part in how the temperature is recorded. Although this has been attempted to be simulated in COMSOL, it varies too much from one stage to the next to be replicated with a constant value. The figures shows a similar, but not identical, thermal response. The simulation has a faster response, likely from the lack of modelling accuracy from tape, screws, thermal contact, etc. However, the total temperature increase is accurate compared to the measured values. This proves a steady state that is similar to the physical setup. The difference in temperature between stage I/II and IV can be explained by sensor error and contact.

After confirming the side core temperature matches that seen in experimental testing, it is also of interest to observe the simulated temperatures around the setup. Figure 4.22 shows the surface temperatures for both air and vacuum at start and simulated end times at 2 h and 4 h, respectively.

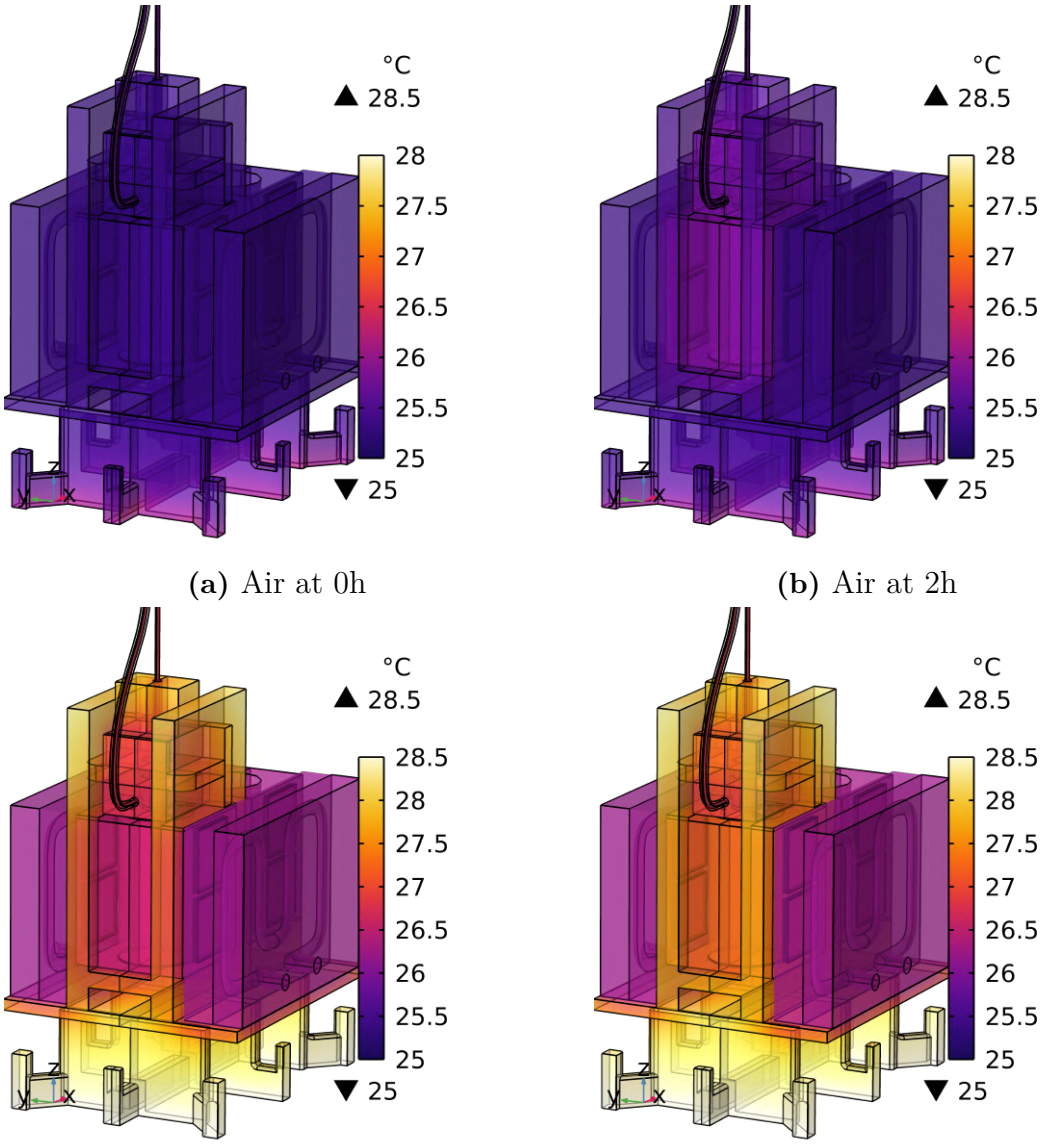

(a) Air at 0h

(b) Air at 2h

(c) Vacuum at 0h

(d) Vacuum at 4h

Figure 4.22: Simulated temperature development at 1W for air and vacuum

Evaluating the temperature evolution over time for the physics-based model, one can see some distinctions between the air and vacuum solutions. For the vacuum solution, only the resistor and aluminium block increase with time, while the heat sink and stand remain steady at their initial temperatures. This aligns well with the temperature measurements taken with the stand's plastic components, where it was observed to be hot both at the bottom and the top. The hot plastic components can therefore also be a underlying factor behind the increase in voltage baseline noticed from experiments.

For the air solution, it can be assessed throughout the simulated calibration to have a more even temperature over the setup. This can be explained by the convection cooling of the system. Concluding that the temperatures seem right, the implications

on the heat flows will be looked at in Chapter 4.4.3.

4.4.2 Simulated voltage

The Peltier elements are simplified in the COMSOL simulation as mentioned in Chapter 3.4.1. The voltage produced from the Seebeck effect in Figure 4.23 is based on the temperature difference from the insides of the ceramic plates of the Peltier elements.

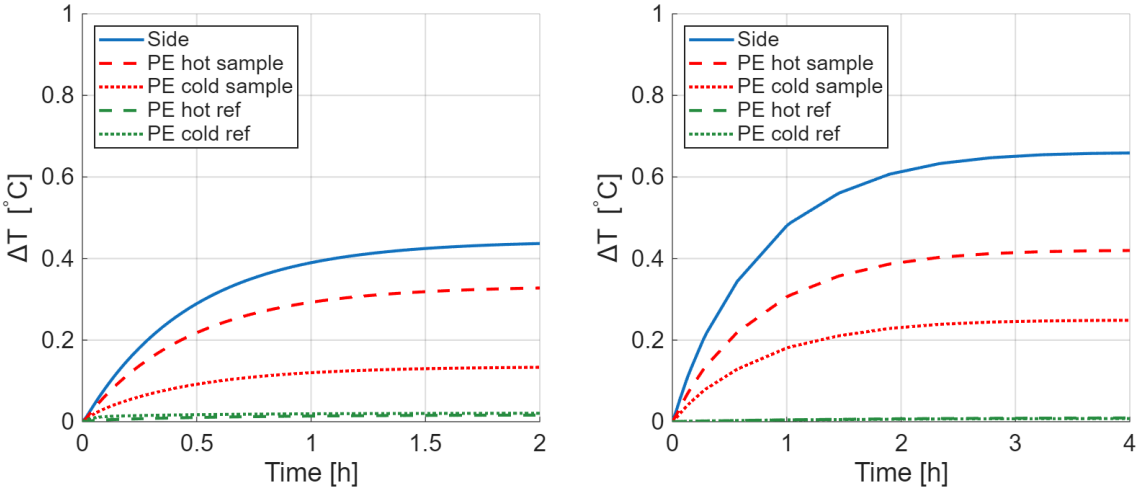

(a) Air **(b)** Vacuum

Figure 4.23: Simulated temperature increase over Peltier elements for air and vacuum

The figure shows that the increase in temperature over the elements is larger in vacuum than in air, as expected with no convective cooling. When comparing the simulated temperature of the side of the core holder, there is around a 2°C difference. Despite this, the difference across the sample's Peltier element is only slightly greater in vacuum than in air. The difference is found to be 0.249°C and 0.257°C for air and vacuum, respectively. A larger temperature difference will result in a higher voltage output from the Peltier elements and thus a lower calibration coefficient.

Based on the datasheet for the Peltier elements, a Seebeck coefficient of 0.2097 V/K is found for the full system. By combining the simulated temperature difference over the Peltier elements with their Seebeck coefficient, a voltage signal is found. This signal is shown in Figure 4.24.

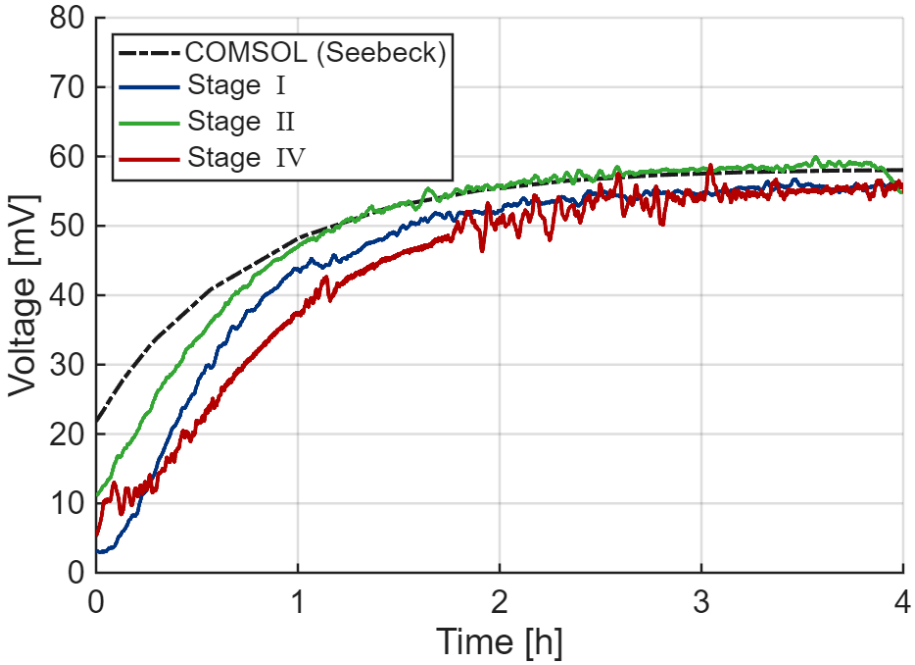

Figure 4.24: Simulated voltage in vacuum based on Seebeck coefficient

The signals shown in Figure 4.24 show two things. It indicates that the modelled simulation can, with good margins, predict the voltage signal created from the Peltier elements from looking at the temperature difference. The only noticeable difference between the numerically solved voltage signal and the one measured from the different stages is that the COMSOL signal starts at a higher starting point. This can be explained by the attempt of trying to get the starting temperatures to match what has been observed.

4.4.3 Heat flow

This section presents a more in-depth look at where the missing heat escapes. To get an idea of how the heat flows, Figure 4.25a and Figure 4.25b showcase with arrow plots how the heat is flowing through the calorimeter in air and vacuum, respectively.

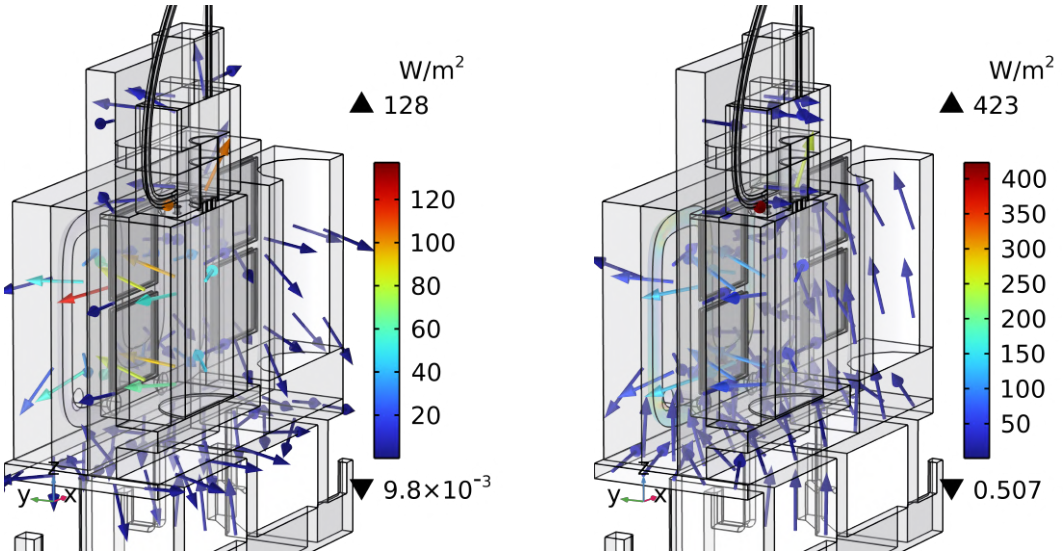

(a) Air **(b)** Vacuum

Figure 4.25: Heat flow arrow plot at 1W over half of the geometry

From Figure 4.25, it is possible to see how the heat flows in and out of the calorimeter setup. For both of these cases, it can be seen that the primary heat flow out from the sample is through the Peltier elements. A major difference is the direction of the heat flow through the stand. In air, the heat flows into the stand since convection helps release the heat from the stand. In vacuum, the heat flow is the opposite. With the chamber walls being hotter than the sample, and no convection is present to cool the stand, the heat will flow from the chamber, through the stand and into the sample holder. To get a better comparison of these heat fluxes, they have been summarised in Table 4.8 where the positive values denote applied/incoming heat and negative denotes heat leaving the resistor.

Table 4.8: Simulated heat flow through the system

Heat Flow	**Air** [mW]	**Vacuum** [mW]
$Q_{Sample\ Applied}$	1000	1000
Q_{PE}	- 794	- 819
Q_{Cables}	- 105	- 217
$Q_{Plastic\ Stand}$	- 48	34
$Q_{Alum.\ Block,\ Convection}$	- 38	0
$Q_{Alum.\ Block,\ Radiation}$	2	2
$Q_{ToT\ Loss}$	- 191	- 217
Extracted Data		
MHFR	79.4%	81.9%
$\eta_{error,\ missing}$	1.78%	0.04%

In Table 4.8, it becomes clearer how the heat is flowing through the system. Analysing the air simulation, the heat is lost through paths including the cables (11%), plastic stand (5%), and convection (3%). In contrast, the vacuum simulation only loses heat through the cables (21%), whereas the plastic stand now heats the aluminium core. The simulations are considered sufficiently accurate, with 1.78% of the heat numerically lost in air and only 0.04% lost in vacuum. This is likely limited by the mesh quality of the simulation.

Vacuum is seen to have more heat flow through the Peltier elements, but also more heat lost through the cables. The MHFR is slightly higher for vacuum, but it falsely quantifies the added heat from the stand and the radiation into the heat flow of the Peltier elements. Since the losses through the cables are twice as much in vacuum as in air, it will be a crucial part of improving the MHFR of the vacuum setup. However, it is also seen that the vacuum successfully removes 38 mW of convective heat losses.

To validate the voltage signals from Figure 4.24 to the model itself, the solved MHFR's are compared. A calibration coefficient can be solved for both air and vacuum simulation, from which an MHFR can be derived. The values for calculating this are shown in Table 4.9.

Table 4.9: Measured Heat Flow Ratio based on simulated ΔT over Peltier elements

Simulation	$\Delta T_{Peltier}$	**Seebeck coefficient**	$\mathbf{U}_{numerical}$	**Power**	$\epsilon_{numerical}$	**MHFR**	$\epsilon_{measured}$
	[°C]	(S) [V/K]	[mV]	[W]	[W/V]	[%]	[W/V]
Air	0.249	0.2097	52.27	1	19.13	79.3	19.93
Vacuum	0.257		53.89		18.56	81.2	19.85

From Table 4.9, the calculated MHFR is simulated to be 79.3% and 81.2% for air and vacuum, respectively. This is close to identical compared to the MHFR based on the heat flow in Table 4.8. The simulated correlation coefficient also matches closely with the measured values, differing by less than 7% for vacuum. This confirms a stable pattern of corresponding values, strengthening the reliability of the digital-twin model.

4.4.4 Cooling

For validating the assumption of turbulent flow inside the heat sink, the velocity, the corresponding Reynolds number and the temperature profile for the circulating cooling water are considered. The velocity and temperature is shown in Figure 4.26, whilst the Re number is calculated from the average velocity.

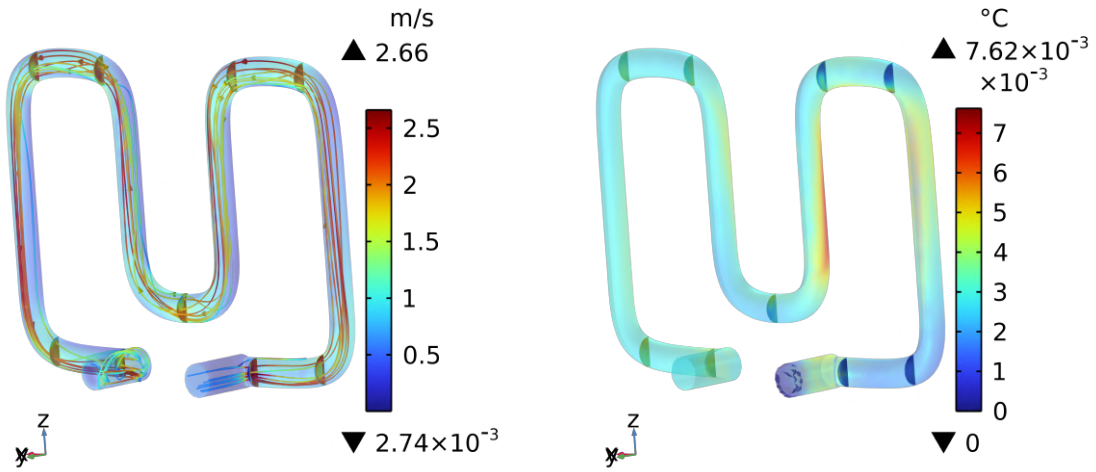

(a) Velocity profile. **(b)** Temperature increase profile.

Figure 4.26: Circulating water velocity and temperature increase inside heat sink at 3.5L/min/heat sink and at 1W

Here, it can be seen that a maximum velocity of 2.66 m/s is reached, with the average velocity being 1.70 m/s. As also noticed from Figure 4.26, the minimum

velocity is 2.74E-3 m/s. This is a simulation result of the water inlet being at the inlet of the heat sink. So to make up for this, it can be said that this is the lowest theoretical water flow inside the heat sink based on the measurements referring back to the results in Table 4.5.

From the average velocity, a Reynolds number of 10 456 can be derived using (2.13) for the inside of the heat sink. This confirms the analysis in Chapter 4.3.5 of having turbulent flow inside the heat sinks. The observed temperature difference of 0.007°C is lower than the estimated theoretical value. However, both estimated temperature increases can be seen as negligible in regard to the Julabo systems' stated cooling power.

Another thing that is also investigated is the radiation onto the heat sinks. Table 4.10 shows theoretical values of radiation onto the heat sink surface utilising Stefan-Boltzmann's law (2.4).

Table 4.10: Comparison of theoretical radiation (Q_{rad}) based on cooling temperature and measured surface temperature of the heat sinks in vacuum

$\mathbf{T}_{cool}$ [°C]	$\mathbf{Q}_{rad}$ [mW]	$\mathbf{T}_{surface}$ [°C]	$\mathbf{Q}_{rad}$ [mW]
15	1180	19	850
25	320	26.5	190
35	-630	33	-430

The calculations are not perfect, as the real surface emissivity and view factors are hard to precisely estimate, yet they show a clear trend. It highlights the huge difference between the various temperatures where the radiative heat contribution reaches roughly 1 W at 15°C. The gap between 15°C and 25°C can be a factor behind the studied trend in Figure 4.19, where the observed heat sink surface temperature was 4°C higher than the input temperature compared to the 1°C difference at 25°C.

The theoretical values can also be compared to the simulated solution. For the simulation, radiation is studied on all surfaces inside the chamber and summarised in Table 4.11. For the table, it denotes positive values as absorbed radiation, while negative denotes reflected radiation. The simulation will provide a more accurate view factor, which is highly relevant for radiation.

Table 4.11: Simulated radiative heating within the chamber for vacuum

Surface	$\mathbf{Q}_{radiation}$ [mW]
Chamber walls	-667
Sample/Reference	13
Heat Sink	172
Plastic Stand	365
Cables	112

From Table 4.11 it can be seen that the radiation onto the heat sink surface matches well with the calculated value of 190 mW from the previous Table 4.10. Looking at Table 4.11, it can also be seen that the radiation is the strongest for the plastic stand. This is followed by the heat sink and cables, with the resistor and reference radiation being less than a tenth of that for the heat sink. These values appear reasonable when observing the individual parts' material surface emissivity and their surface areas. Combining all the absorbed heat, 662 mW, there is less than a 1% difference in the total balance. This confirms the numerical conservation of thermal radiation within the model.

4.4.5 Temperature dependency

As noticed from the experimental observations, the temperature of both the chamber and the heat sink has been analysed to play a huge part in the measured heat flows. So to investigate this further, the temperature of the chamber was swept for the vacuum model. The Table 4.12 displays the observed heat flows at each of these temperatures where the water cooling was kept at 26°C.

Table 4.12: Heat flow of swept cooling temperature in vacuum

Heat Flow	**Vacuum 23.5°C** [mW]	**Vacuum 25°C** [mW]	**Vacuum 28.5°C** [mW]	**Vacuum 30°C** [mW]
$Q_{Sample\ Applied}$	1000	1000	1000	1000
Q_{PE}	- 623	- 675	- 819	- 863
$Q_{Elec.\ Comp.}$	- 192	- 194	- 217	- 212
$Q_{Plastic\ Comp.}$	- 170	- 109	34	84
$Q_{Alum.\ Block,\ Radiation}$	- 9	- 6	2	5
$Q_{ToT\ Loss}$	- 371	309	- 181	- 123
Extracted Data				
MHFR	62.3%	67.5%	81.9%	86.3%
$\eta_{error,\ missing}$	0.6%	1.7%	0.04%	1.4%

From Table 4.12, a clear trend can be seen where a higher vacuum temperature results in a higher observed MHFR, or in other terms, a lower calibration coefficient. This is an expected trend from the observations, as the warmer chamber will disperse more heat onto the calorimeter, both through radiation from the walls and through conduction in the stand. It is shown that the heat flow through the Peltier elements is the highest at 30°C. However, with the uncontrollable contribution from the stand and the radiation also increasing, the increased heat flow would not be from the sample source alone, proving that balance is more important for isolating the true heat flow.

The table also supports the previously mentioned theory of a temperature that provides thermal equilibrium and a 0 mV baseline. In fact, the table narrows down the ideal temperature from between 25-35°C to between 25-28.5°C. This would mean that the contribution from the stand and radiation is both 0 mW, leaving only the parasitic losses through the cables. The model would still be subject to a shifting baseline, following the lab temperature, but the initial losses would be greatly reduced.

4.4.6 Accuracy and validation

To numerically validate the model, a mesh independence study was conducted on the vacuum. This is carried out to see how much of the solution revolves around the numerical structure and how much the physics gets dimmed by the structure of the mesh. To do this model validation, a finer mesh than that used was created and used to compare temperatures on the side of the aluminium block as well as comparing the heat flow through the Peltier elements, as well as the cables, stand, and radiation onto the aluminium block. Table 4.13 shows the differences between the two meshes.

Table 4.13: Mesh used for mesh independence study

Mesh	**Number of Elements**	**Simulation time**
Used Mesh	625 195	9 min 52 s
Finer Mesh	1 420 983	13 min 38 s

From Table 4.13, the finer mesh created has more than double the number of elements as the one used. This resulted in the solution time for the finer mesh to increase by about 4 min. To study the numerical impact the increase in elements has on the solution, the change in surface temperature between the two meshes was first looked at. Figure 4.27 shows this over the geometry as changes in temperature over the system between the two different meshes as $\Delta T = T_{finer} - T_{used}$.

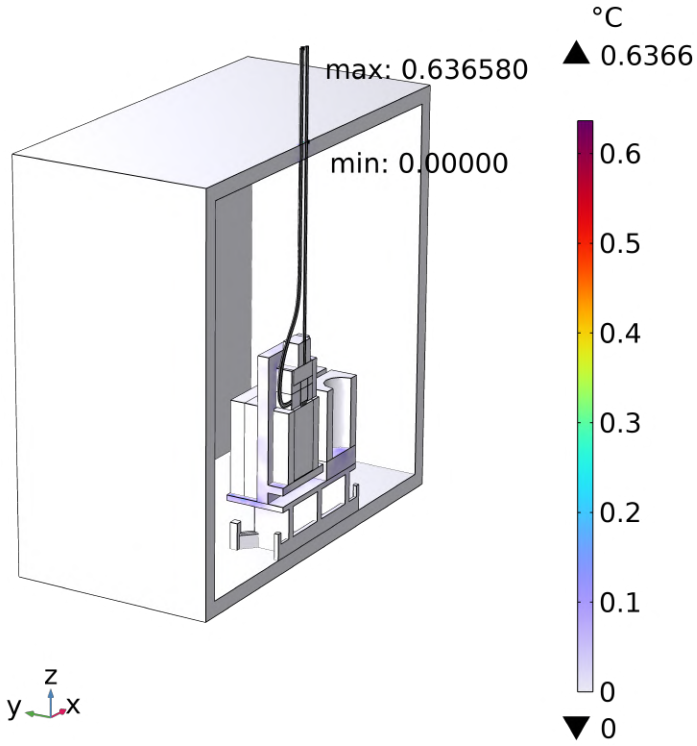

Figure 4.27: Mesh independence study results for surface temperature change between meshes

From Figure 4.27, it can be seen that no major temperature changes occur with a finer mesh. The highest temperature difference, 0.637 °C, occurs at the top of cables and is a result of the mesh being more fit for the circular edge. However, as this change occurs outside the simulation's study scope and is within the acceptable difference for this thesis, this is deemed acceptable. For further mesh independence validation, some important heat flows are also looked at, which can be seen in Table 4.14.

Table 4.14: Verification of mesh independence through heat flow

Mesh	**Peltier elements**	**Cables**	**Plastic components**	**Alum. block radiation**
	[mW]	[mW]	[mW]	[mW]
Used Mesh	-819	-217	34	2.1
Finer Mesh	-817	-216	34	2.0
Difference	1.7	0.7	0.0	0.1

The heat flow differences are a maximum of 4.8% change for the incoming radiation. Though this percentage difference is quite significant, the resulting heat of only 0.1

mW is overlooked. To weigh between computational accuracy and computational cost, the mesh used is seen to be within an acceptable difference.

4.5 Sources of error

Experimental laboratory work is rarely perfect and is prone to errors. This section aims to identify the most significant mistakes and inaccuracies.

In a vacuum, the help to bridge the heat transfer in microscopic gaps is gone. Conduction and radiation are the only sources of heat transfer. This means that the physical connection between components is crucial. The PT100 sensors were especially sensitive to changes in the thermal connection. As previously mentioned, attempts were made to investigate the optimal solution, without a clear answer. It is expected that the connection and behaviour of the sensors in vacuum make up an uncertainty that can not be ignored for accurate measurements. However, since the heat flow through the Peltier elements was deemed more important, it was not prioritised to quantify this uncertainty.

There will always be an inaccuracy in the measuring equipment used as shown in Appendix A.2. However, as the listed accuracies for the equipment were relatively small, and as they are unpredicted they were neglected in the results. Though the uncertainty can't be sufficiently fixed for, the analysed trends were still observed which was reflected as the most important part.

The cooling system of the setup was initially thought to be over-dimensioned and thus not considered as a source of error. Although the pump is assumed to have sufficient power, the skewed placement of the T-connection meant unequal cooling for the heat sinks. This is an error that has been investigated and considered for the results.

There was an attempt to quantify the effect of the lab temperatures on the vacuum chamber. Although a clear correlation was discovered, it is difficult to reveal what the true source of this heat flow is. A likely source is parasitic heat that follows the cables and sensors into the chamber. Since it was proven that the inside of the chamber is hotter than the setup, it can be assumed that sensors and cables absorb some of this heat at their entry-point into the chamber. The unwanted heat flow from the surroundings can have an effect on the recorded temperatures, and in the worst case, contribute heat to the setup.

Unwanted heating proved to be an issue with the vacuum chamber. Radiative heating has been underestimated when designing the setup. Especially when the temperature of the cooling liquid was lowered, the heat sink surfaces experienced a significant temperature rise. Although it is difficult to physically confirm the source of the heating, the theory and simulation support the theory of unwanted radiative heating.

There is also a chance that the use of the reference cell was not done sufficiently.

Although it appeared to be helpful to isolate the true heat flow of the sample, the reference cell itself did not represent the sample setup completely. The 3D printed plastic stand that held the sample cell in place was missing for the reference cell. As both recorded and simulated values show, the plastic holder heated up significantly and was contributing heat flow into the aluminium sample cell holder.

5

Conclusion

This chapter will present the final conclusions that are drawn from the results of this report. The focus will primarily be on the quantification and usefulness of the vacuum chamber. Additionally, the conclusions aim to connect the physical data to the simulated, verifying whether the simulation is useful. Future work will be presented to help improve a potential future continuation of the work.

5.1 Results from present work

Vacuum was introduced as a thermal isolator, and it proved highly effective in eliminating heat loss through convection, although it made the testing process significantly more time-consuming. While the system reaches a steady state in air in under 2 hours, the vacuum environment requires nearly 6 hours to achieve a similar level of stability. The increased time constant is directly linked to the thermal resistance, which increases when convection is no longer present. This results in the maximum temperature being 1°C higher in vacuum than in air. To ensure accurate results, it was found that the use of a reference cell and baseline voltage corrections is beneficial for isolating the true thermal response of the sample.

The system's sensitivity was found to be between 50 mW and 100 mW. While signals at 50 mW were detectable, fluctuations made them too unreliable for calibration. For power levels exceeding 1 W, the average calibration coefficient (ϵ) was found to be 19.93 and 19.85 W/V for air and vacuum, respectively. At power levels under 1 W, radiative heating and unforeseen heat sources gradually drowned out the voltage signal. At higher power levels, the heat from the sample cell overcomes the heat losses and indicates the potential of vacuum achieving a lower calibration coefficient.

This instability is closely related to the high correlation observed between the laboratory temperature and the internal chamber environment. It appears that the ambient lab temperature directly warms the chamber walls, which then act as a primary source of radiative heat. This effect gets increasingly problematic if the cooling temperature is lowered. Experimental data suggest that there is a thermal equilibrium with a baseline of 0 mV when the cooling is set between 25°C and 35°C. However, because of the direct influence of the lab surroundings, this equilibrium is not fixed and changes throughout the testing period.

The cooling system was found to have a flow rate of 6.5 L/min, which meant that turbulent flow is present. Yet, the heat sink design proved to be challenging for thermal stability. The chamber walls at 28-30°C create a distinct radiative contribution, which increases with colder heat sinks. This is most critical at 15°C cooling, where the average ΔT of the heat sink surface reaches 3.96°C in vacuum. That is nearly six times the offset observed at 25°C (0.70°C). The heat sinks remain more stable in air, as convection helps them remain cool. The 40/60 flow split from the tilted T-connection adds to the instability of the heat sinks, which motivates a redesign to maintain a reliable cold-side reference for the Peltier elements.

The development of a physics-based digital twin provided important insights into the heat pathways of the system. The model was validated against experimental data with only a 7% deviation in heat leakage. A key finding from the simulation was that the power cables act as parasitic heat paths in vacuum, pulling away 21% of the applied heat from the sample cell, twice as much as in air. In vacuum, the heat contribution from the stand and radiation returns a falsely high MHFR of 81.9%. Furthermore, both the simulation and the theory agree that the heat sinks receive 170-190 mW of radiative heat. These numerical results confirm that the current calorimeter's performance is mainly limited by radiation and parasitic cable conduction rather than a lack of cooling power.

5.2 Implications for Battery Calorimetry

The primary objective of this project was to develop a calorimeter suitable for battery testing, and the obtained results provide a clear direction for its practical application. Implementing a vacuum environment is beneficial for battery calorimetry, as eliminating convective losses ensures that the heat generated is more effectively captured by the Peltier sensors. The established sensitivity of 50-100 mW is close to being sufficient, as the cell is estimated to produce 30-800 mW of heat in a range of 0.1C to 0.5C. However, the 1 W limit for a stable calibration coefficient (ϵ) suggests that the current configuration is best suited for testing higher C-rates with distinct heat generation.

For high-precision characterisation of internal heat generation, the parasitic heat paths found in the digital twin serve as crucial correction factors. The 20% heat leakage through the power cables and the 30-80 mW contribution from the plastic stand must be included in an energy balance to avoid underestimating the battery's thermal response. The 6-hour time constant contradictory indicates that the high C-rate tests must be performed over a sufficiently long time. To improve the calorimeter's adaptation to a battery cell, the time constant should be reduced by increasing thermal contact with the Peltier elements and reducing the thermal mass of the system. To enhance the sensitivity of the system, future testing should prioritise matching the coolant temperature to the ambient chamber temperature to achieve a 0 mV baseline. Using the Tian correction could also be beneficial for pulse or high C-rate testing, to avoid the need for thermal stabilisation.

5.3 Future Work

Regarding the conclusions drawn in the report, continued work is needed to optimise and perfect the setup and the digital twin. Although the list of potential changes and improvements is extensive, this section focuses on the changes that are assumed to have the most impact on the setup.

- **Reducing radiative heat** will be crucial for the success of the vacuum environment. To eliminate radiation, the temperature difference between the chamber and the surroundings must be reduced. By painting, coating or isolating the calorimeter, it will absorb less radiation from the chamber walls. A radiative shield around the setup could also be thermally connected to the heat sinks, disrupting the direct line-of-sight while remaining cold.

- **Improving the cooling capacity** will provide the calorimeter with a stable cold side reference for the Peltier elements, which is crucial for isolating the generated heat response. A rewired tube setup or a Y-connection would make for equal cooling to each heat sink. By making the heat sinks thinner and changing the internal flow to many small channels, the cooling power would disperse more effectively, keeping the surface closer to the cooling temperature. Alternatively, a heat sink in copper will have double the thermal conductivity of the current aluminium, which will increase the cooling effect of the water.

- **Achieving thermal equilibrium** will likely improve the sensitivity of the setup, making it useful for smaller heat flows. Since a high correlation was proven between the lab and chamber temperature, matching the cooling temperature to the lab temperature will keep the setup and chamber at a similar temperature. This will have new issues with long time constants and a shifting equilibrium, but it could potentially reduce a significant amount of baseline noise.

- **Optimising the thermal contact** of the Peltier elements will increase the MHFR, as more heat is allowed to flow through. This can be achieved by changing the thermal gap pads to a new pad or paste with a higher thermal conductivity. By reducing the thermal resistance to the Peltier elements, the time constant can also be reduced. Optimising contact can also include switching to flexible Peltier elements, which greatly reduces the time constant and allows for the recording of the thermal gradient along the sample surface.

- **Minimising parasitic cable conduction** is essential, as the digital twin revealed that electrical cables account for about 20% of the total heat leakage in vacuum. Wires should be optimised for a low thermal conductivity while remaining sufficient for the conduction of current. Cables and sensors can also be thermally anchored by being grounded to the heat sinks before being attached. This would ensure that any heat entering through the cables is diverted to the cooling system rather than the setup.

- **Improving reference cell symmetry** is necessary to ensure that the mea-

surement accurately isolates environmental noise. Currently, the reference cell does not have the 3D-printed plastic stand used for the sample holder, which was found to contribute 30–80 mW of heat in vacuum. Creating an equal thermal mass for the sample and the reference will improve the reliability of the net heat flow calculation, further improving the stability of the calibration coefficient.

- **Optimising sensor attachment** would significantly reduce measurement uncertainty. The current use of Kapton tape proved unreliable in vacuum, leading to poor thermal contact and an observed temperature offset of up to 1°C between sensors. For optimal accuracy, permanently integrating sensors into the setup will provide sufficient thermal contact and reduce radiative heat. Improving the accuracy of the temperature measurements will be important for further developing the digital-twin model.

- **Improving the physics-based model** can be valuable in further discovering parasitic heat losses and efficiently improving the setup. The current model can be used to see the effect of changes in power, temperature, material selection, etc. With further improvements to the mesh, an increased accuracy can be achieved. The model will also be highly useful for investigating the internal heat generation of a battery cell.

Bibliography

[1] Thomas Fugger, Joseph Poligkeit, and Christoph Herrmann. "Decarbonization in the Automotive Sector: A Scenario-based Analysis of Original Equipment Manufacturer Pathways". In: *Cleaner Environmental Systems* 19 (Dec. 2025). DOI: 10.1016/j.cesys.2025.100336.

[2] Matteo Muratori et al. "The rise of electric vehicles—2020 status and future expectations". In: *Progress in Energy* 3.2 (Mar. 2021), p. 022002. DOI: 10.1088/2516-1083/abe0ad. URL: https://doi.org/10.1088/2516-1083/abe0ad.

[3] Minseok Song et al. "Analysis of the Heat Generation Rate of Lithium-Ion Battery Using an Electrochemical Thermal Model". In: *Journal of the Electrochemical Society* 167 (Aug. 2020). DOI: 10.1149/1945-7111/aba96b.

[4] Wenlin Yuan et al. "Self-calibrated calorimetry to minimize the measurement uncertainty of the specific heat and heat generation rate for prismatic batteries". In: *International Journal of Heat and Mass Transfer* 247 (Sept. 2025), p. 127172. DOI: 10.1016/j.ijheatmasstransfer.2025.127172.

[5] Yixin Dai and Aidin Panahi. "Thermal runaway process in lithium-ion batteries: A review". In: *Next Energy* 6 (Jan. 2025), p. 100186. DOI: 10.1016/j.nxener.2024.100186.

[6] Yang Hu, Song-Yul Choe, and Taylor R Garrick. "Measurement of two-dimensional heat generation rate of pouch type lithium-ion battery using a multifunctional calorimeter". In: *Journal of Power Sources* 532 (2022), p. 231350.

[7] Satyam Panchal et al. "Design and simulation of a lithium-ion battery at large C-rates and varying boundary conditions through heat flux distributions". In: *Measurement* 116 (2018), pp. 382–390.

[8] Daniel Worwood et al. "A new approach to the internal thermal management of cylindrical battery cells for automotive applications". In: *Journal of Power Sources* 346 (Apr. 2017), pp. 151–166. DOI: 10.1016/j.jpowsour.2017.02.023.

[9] SJ Drake et al. "Heat generation rate measurement in a Li-ion cell at large C-rates through temperature and heat flux measurements". In: *Journal of Power Sources* 285 (2015), pp. 266–273.

[10] KA Murashko et al. “Determination of the entropy change profile of a cylindrical lithium-ion battery by heat flux measurements”. In: *Journal of Power Sources* 330 (2016), pp. 61–69.

[11] Lei Sheng et al. “A calibration calorimetry method to investigate the thermal characteristics of a cylindrical lithium-ion battery”. In: *International Journal of Thermal Sciences* 165 (July 2021), p. 106891. DOI: 10.1016/j.ijthermalsci.2021.106891.

[12] Joanna Kozma et al. “Direct measurement of heat generation in a cylindrical Li-ion battery using heat flux sensors”. In: *Journal of Power Sources* (2026). URL: https://api.semanticscholar.org/CorpusID:284768430.

[13] Qingsong Wang et al. “Environmental Impact Analysis and Process Optimization of Batteries Based on Life Cycle Assessment”. In: *Journal of Cleaner Production* 174 (Nov. 2017). DOI: 10.1016/j.jclepro.2017.11.059.

[14] M. Lybbert et al. “Integrating life cycle assessment and electrochemical modeling to study the effects of cell design and operating conditions on the environmental impacts of lithium-ion batteries”. In: *Renewable and Sustainable Energy Reviews* 144 (2021), p. 111004. ISSN: 1364-0321. DOI: https://doi.org/10.1016/j.rser.2021.111004. URL: https://www.sciencedirect.com/science/article/pii/S136403212100294X.

[15] Pratima Meshram and Dr Abhilash. “Environmental Impact Assessment in the Entire Life Cycle of Lithium-Ion Batteries”. In: *Reviews of Environmental Contamination and Toxicology* 262 (Jan. 2024). DOI: 10.1007/s44169-023-00054-w.

[16] Institute of Electrical and Electronics Engineers (IEEE). *IEEE Policies, Section 7 - Publications*. https://www.ieee.org/about/corporate/governance/p7-8. Accessed: 2026-04-25. 2026.

[17] Anton Lidbeck and Kazim Raza Syed. “Experimental Characterization of Li-ion Battery cells for Thermal Management in Heavy Duty Hybrid Applications”. Division of Electric Power Engineering. Master’s thesis. Gothenburg, Sweden: Chalmers University of Technology, 2017.

[18] James R. Welty, Gregory L. Rorrer, and David G. Foster. *Fundamentals of Momentum, Heat, and Mass Transfer*. 7th. John Wiley & Sons, 2019. Chap. 15.

[19] James R. Welty, Gregory L. Rorrer, and David G. Foster. *Fundamentals of Momentum, Heat, and Mass Transfer*. 7th. John Wiley & Sons, 2019. Chap. 23.

[20] Vac coat. *Outgassing | What is Outgassing in Vacuum Chamber?* Accessed: 2026. URL: https://vaccoat.com/blog/what-is-outgassing-in-vacuum-chamber/.

[21] J Rothka et al. “Outgassing of silicone elastomers”. In: *ARLON–Silicone Technol Div Bear* 19701 (2002).

[22] Frank P. Incropera et al. *Principles of Heat and Mass Transfer*. 7th. International student version. Wiley, 2013. Chap. 5, pp. 280–283.

[23] Robert A. Huggins. *Advanced Batteries: Materials Science Aspects*. Focuses on the thermodynamics of electrochemical cells, including entropy and the Gibbs-Helmholtz equation. Springer Science & Business Media, 2008. ISBN: 978-0-387-76423-8.

[24] Marco Nesarajah and Georg Frey. "Thermoelectric power generation: Peltier element versus thermoelectric generator". In: *IECON 2016 - 42nd Annual Conference of the IEEE Industrial Electronics Society*. 2016, pp. 4252–4257. DOI: 10.1109/IECON.2016.7793029.

[25] G. Prunet et al. "A review on conductive polymers and their hybrids for flexible and wearable thermoelectric applications". In: *Materials Today Physics* 18 (2021), p. 100402. ISSN: 2542-5293. DOI: https://doi.org/10.1016/j.mtphys.2021.100402. URL: https://www.sciencedirect.com/science/article/pii/S2542529321000638.

[26] Andrew Mandeya. "Heat Generation Analysis of Lithium-Ion Pouch Cells using Calorimetric Methods". Loss verification of Li-Ion battery cell from thermal flow measurements. Master's thesis. Gothenburg, Sweden: Chalmers University of Technology, 2023.

[27] Bengt Andersson et al. *Computational Fluid Dynamics for Engineers*. Cambridge, UK: Cambridge University Press, 2012. Chap. 4. ISBN: 978-1107018952.

[28] Lars Wadsö. "Operational issues in isothermal calorimetry". In: *Cement and Concrete Research* 40.7 (2010), pp. 1129–1137. ISSN: 0008-8846. DOI: https://doi.org/10.1016/j.cemconres.2010.03.017. URL: https://www.sciencedirect.com/science/article/pii/S0008884610000864.

[29] IPETRONIK GmbH & Co. KG. *M-RTD2 Datasheet*. 4 PT100 measurement inputs. 2025. URL: https://www.ipetronik.com.

[30] IPETRONIK GmbH & Co. KG. *M-SENS 8plus Datasheet*. 8-channel analog measurement module. URL: https://www.ipetronik.com.

[31] Keysight Technologies. *EDU36311A Triple Output Bench Power Supply Datasheet*. 2021. URL: https://www.keysight.com.

[32] ARCOL UK Limited. *HS Aluminium Housed Resistors Datasheet*. Model HS100, 15 Ohm Power Resistor. 2008. URL: https://www.arcolresistors.com.

[33] European Thermodynamics Limited. *GM250-127-14-10 Thermoelectric Generator Module Datasheet*. 2017. URL: https://www.etdyn.com.

[34] JULABO GmbH. *CORIO CD-200F Refrigerated/Heating Circulator*. Accessed: 2026. URL: https://www.julabo.com/en/products/refrigerated-circulators/refrigerated-heating-circulators/corio-cd-200f.

[35] Harald Peters. *Pt100 sensors - accuracy classes of resistance thermometer*. https://www.pt100.de/EN/EN-pt100-accuracy.html. Besøkt: 28. april 2026. 2024.

[36] George EP Box. "Science and statistics". In: *Journal of the American Statistical Association* 71.356 (1976), pp. 791–799.

[37] David Michael Rowe. *CRC Handbook of Thermoelectrics*. CRC Press, 2018.

A

Appendix

A.1 Theoretical calculation - calibration coefficient

For calculating the theoretical calibration coefficient ($\epsilon_{theoretical}$) equations presented in Chapter 2.5 are used estimating a mean temperature at $25°C$.

Following (2.15), (2.16), (2.19) and (2.21) for sett mean temperature the Seebeck coefficient for the set-up system is calculated .
Seebeck coefficient n-legs is $\alpha_n(T) = (0.001530736 \times 25^2 - 1.08058874 \times 25 - 28.338095) \times 10^{-6} = -2.144 \times 10^{-4}$V/K
Seebeck coefficient p-legs is $\alpha_p(25°C) = (-0.003638095 \times 25^2 + 2.74380952 \times 25 - 296.214286) \times 10^{-6} = 1.985 \times 10^{-4}$V/K
Seebeck coefficient for one peltier element (module) is than $S_{module} = 127(1.985 \times 10^{-4} - (-2.144 \times 10^{-4}) = 0.0524$V/K
Set-up seebeck coefficient is then $S_{system} = 4 \times 0.0524 = 0.2097$V/K

The same using (2.17), (2.18), (2.20) and (2.22) at set mean temperature will derive the thermal conductivity of the set-up through the peltier elements.
Thermal conductivity n-legs is $k_n(25°C) = 0.0000334545 \times 25^2 - 0.023350303 \times 25 + 5.606333 = 1.618$W/mK
Thermal conductivity p-legs is $k_p(25°C) = 0.0000361558 \times 25^2 - 0.026351342 \times 25 + 6.22162 = 1.579$W/mK
Thermal conductivity for one peltier element (module) is than $K_{module} = 127(1.618 - 1.579)\dfrac{0.0014 \times 0.0014}{0.001} = 0.7958$W/K
Set-up thermal conductivity is then $K_{system} = 4 \times 0.7858 = 3.143$V/K

Lastly, using the calculated values in (2.23) gives $\epsilon_{theoretical} = \dfrac{3.143}{0.2097} = 15.178$W/V

A.2 Uncertainty calculation - calibration coefficient

For variables u, x, y and z with known uncertainty and the measured value is computed

$$v = \frac{u \times x}{y \times z}$$

then if the uncertainty of x, ..., z are measured with uncertainty δx, ..., δz and it's known that the uncertainty of these variables are independent and random. Then by the uncertainty of quadrature method the value of v uncertainty is quadrature of original fractional uncertainty,

$$\frac{\delta v}{|v|} = \sqrt{\left(\frac{\delta x}{|x|}\right)^2 + \left(\frac{\delta y}{|y|}\right)^2 + \left(\frac{\delta z}{|z|}\right)^2}$$

Example calculation for uncertainty of calibration coefficient at $0.5W$:

The readback accuracy of Keysight EDU36311A, according to the datasheet, gives the following uncertainties.

Input voltage: V = $2.769V$
Uncertainty in voltage inlet: $\delta V = 0.05\% \times 2.769 + 0.010 = 0.01138V$
Input current: I = $0.180A$
Uncertainty in current input: $\delta I = 0.2\% \times 0.180 + 0.005 = 0.00536A$

Then from these inputs, the power applied to the heater: $P = V \times I = 0.498W$
whit an uncertainty $\delta P = 0.49842 \times \sqrt{\left(\frac{0.011384}{|2.769|}\right)^2 + \left(\frac{0.00536}{|0.180|}\right)^2} = 0.01498W$

As per Table 3.1, the M-SENS 8plus have an uncertainty of 0.06%.
Measured voltage signal: U = 0.02612
The measured voltage uncertainty $\delta U = 0.06\% \times U = 0.00001567V$

Calibration coefficient $\epsilon = \frac{P}{U} = 19.082$.
Than the uncertainty for the calibration coefficient
$\frac{\delta\epsilon}{\epsilon} = \sqrt{\left(\frac{0.01498}{|0.498|}\right)^2 + \left(\frac{0.00001567}{|0.02612}\right)^2} = 3.01\%$

A.3 COMSOL physics

Table: Applied physics, multiphysics coupling and boundary conditions for models

Physics module	**Model**	**Multiphysics coupling**	**Boundary conditions**
Turbulence flow, $k-\varepsilon$	Air & Vacuum	Nonisothermal flow	Fluid properties Initial values Wall Inlet Outlet
Heat transfer solid & fluids	Air & Vacuum Air Vacuum	Nonisothermal flow Heat transfer with surface-to-surface radiation	Solid 1 Fluid Initial values Inflow Outflow Temperature Thin layer Solid 2 Heat flux Surface-to-ambient radiation
Surface-to-surface radiation	Vacuum	Heat transfer with surface-to-surface radiation	Initial values Diffuse surface
Electric currents	Air & Vacuum	Joule heating	Current conservation Electric insulation Initial values Terminal Ground

DEPARTMENT OF SOME SUBJECT OR TECHNOLOGY
CHALMERS UNIVERSITY OF TECHNOLOGY
Gothenburg, Sweden
www.chalmers.se

CHALMERS
UNIVERSITY OF TECHNOLOGY